JGR Space Physics

RESEARCH ARTICLE

10.1029/2021JA030157

Key Points:

- Traveling Ionospheric Disturbances partially modulate SuperDARN Near Range Echoes
- Zonal wind and meridional convection electric field produce Gradient Drift Instabilities observed as Near Range Echoes in the *E*-region
- Traveling Ionospheric Disturbances propagating in the *F*-region partially modulate the Gradient Drift Instabilities

Supporting Information:

Supporting Information may be found in the online version of this article.

Correspondence to:

M. J. Kosch and A. Hiyadutuje,
mkosch@sansa.org.za;
hiyadutujea@yahoo.fr

Citation:

Hiyadutuje, A., Kosch, M. J., & Stephenson, J. A. E. (2022). First observations of *E*-region Near Range Echoes partially modulated by *F*-region Traveling Ionospheric Disturbances observed by the same SuperDARN HF radar. *Journal of Geophysical Research: Space Physics*, *127*, e2021JA030157. https://doi.org/10.1029/2021JA030157

Received 25 NOV 2021
Accepted 10 APR 2022

Author Contributions:

Data curation: Alicreance Hiyadutuje
Formal analysis: Alicreance Hiyadutuje
Investigation: Alicreance Hiyadutuje
Methodology: Alicreance Hiyadutuje, Michael J. Kosch, Judy A. E. Stephenson
Supervision: Michael J. Kosch, Judy A. E. Stephenson
Writing – original draft: Alicreance Hiyadutuje
Writing – review & editing: Michael J. Kosch, Judy A. E. Stephenson

First Observations of *E*-Region Near Range Echoes Partially Modulated by *F*-Region Traveling Ionospheric Disturbances Observed by the Same SuperDARN HF Radar

Alicreance Hiyadutuje[1,2], Michael J. Kosch[1,2,3,4], and Judy A. E. Stephenson[2]

[1]South African National Space Agency, Hermanus, South Africa, [2]Department of Chemistry and Physics, University of KwaZulu-Natal, Durban, South Africa, [3]Department of Physics and Astronomy, University of Western Cape, Cape Town, South Africa, [4]Department of Physics, University of Lancaster, Lancaster, UK

Abstract We present the first observations from SuperDARN HF radar data of *E*-region Near Range Echoes (NREs) whose amplitudes are partially modulated by Medium-Scale Traveling Ionospheric Disturbances (MSTIDs) propagating in the *F*-region overhead that have been observed by the same radar in the far ranges. SuperDARN NREs occur normally ~180–315 km downrange from the radar at ~95–125 km altitude. Selected observations of TID-modulated NREs are presented from SANAE and Zhongshan Antarctic SuperDARN radars for both summer and winter seasons as well as geomagnetic active and quiet times. We show that the most likely mechanism is partial modulation of the Gradient Drift Instability (GDI), which is responsible for producing the NREs. GDI is driven by the velocity difference between neutrals and ions and may appear in the *E*-region ionosphere wherever suitable plasma density gradients exist. GDI already present in the *E*-region can be partially modulated by an MSTID passing overhead in the *F*-region via the additional MSTID polarization electric field mapped down in altitude along the equipotential magnetic field lines, thereby partially modulating the NRE amplitudes as observed.

1. Introduction

Atmospheric Gravity Waves (AGWs) carry significant momentum and energy throughout the Earth's atmosphere (Francis, 1975; Fritts, 1984; Hunsucker, 1982) and may be observed in the upper atmosphere by the SuperDARN global network of radars (Chisham et al., 2007; Oinats et al., 2015) as Traveling Ionospheric Disturbances (TIDs) through the interaction between the neutral and ionized components of the atmosphere. However, TIDs may also be driven by ionospheric electric fields via the Perkins instability at nighttime (Y. Liu et al., 2019, and reference therein). TIDs may be observed in the ionospheric *F*-region 30%–50% of the time (Francis, 1974). TIDs are divided into two main classes: Large-Scale Traveling Ionospheric Disturbances (LSTIDs) with horizontal wavelengths of >1,000 km, velocities of ~400–1,000 m/s, and periods of ~0.5–3 hr and Medium-Scale Traveling Ionospheric Disturbances (MSTIDs) with horizontal wavelengths of hundreds of km, velocities of ~100–500 m/s, and periods of ~15–60 min (Grocott et al., 2013; Hayashi et al., 2010; He et al., 2004; Hocke & Schlegel, 1996; Oinats et al., 2015). The many possible AGW/TID sources and their propagation modes have been investigated (e.g., Hocke & Schlegel, 1996; He et al., 2004; Grocott et al., 2013). LSTIDs are generated in the auroral or sub-auroral region as a result of Lorentz forces and Joule heating caused by the enhancement of the auroral electrojets and/or intense precipitation of charged particles during geomagnetic storms (Ding et al., 2008; Palmroth et al., 2005; Waldock & Jones, 1986). Storm-induced TIDs usually propagate equatorward from high latitudes and sometimes cross the equator (Ding et al., 2008; Habarulema et al., 2015; Tsugawa et al., 2004). MSTIDs are the most common at high latitudes, often caused by the auroral electrojets, and may propagate horizontally, obliquely, or vertically in the ionosphere (Hocke & Schlegel, 1996). They may propagate from the source either obliquely up to the *F*-region or initially downward and reach the *F*-region after the reflection from the ground (Francis, 1974; Hernández-Pajares et al., 2006). High-latitude MSTIDs have been observed propagating equatorward (Grocott et al., 2013; Samson et al., 1990), westward (Samson et al., 1990), and poleward (Habarulema et al., 2015). At southern high latitudes, the probability of medium-scale AGW observations was highest in winter and lowest in summer months (Ogawa et al., 1987) but they may occur at any time.

SuperDARN is a global network of HF radars (Chisham et al., 2007; Greenwald et al., 1995) that normally observe Bragg backscatter from magnetic field-aligned plasma irregularities (FAIs), which are common in the

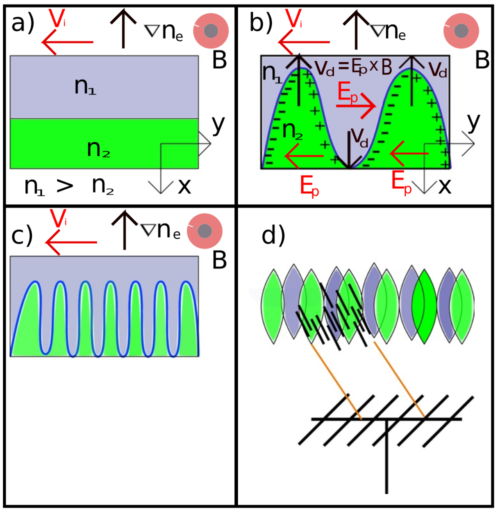

Figure 1. A cartoon showing how a plasma density disturbance in the southern hemisphere may result in radar coherent backscatter via the Gradient Drift Instability mechanism (adapted from Gillies (2012)). The magnetic field (**B**) is out of the page. Panel (a) shows two stable layers with plasma densities $n_1 > n_2$. In the *E*-region, the ionospheric electric field will be approximately parallel to the ion velocity ($\mathbf{V}_\mathrm{i}$). In the *F*-region, due to convection, the ionospheric electric field will be approximately parallel to the plasma density gradient (∇n_e). Panel (b) shows any wave-like perturbation on the plasma boundary, will result in a charge separation, and an oscillating polarization electric field ($\mathbf{E}_\mathbf{p}$). $\mathbf{E}_\mathbf{p}$ drives a plasma drift ($\mathbf{V}_\mathbf{d}$) that grows the plasma perturbation. Panel (c) shows the time development of the plasma perturbation, cascading to shorter wavelengths. Panel (d) shows the coherent scatter by these plasma structures once the Bragg scatter condition is met.

F-region ionosphere, for ray paths that satisfy the necessary aspect condition (Ruohoniemi et al., 1989). SuperDARN radars also observe backscatter from the ground or sea surfaces due to HF refraction in the ionosphere. The SuperDARN radars readily detect MSTIDs as wave-like perturbations in the backscatter (Chisham et al., 2007; Hunsucker, 1982; Miyoshi et al., 2018; Nishitani et al., 2019), typically in the range of ∼600–1,200 km. MSTIDs are either observed in the ground/sea scatter echoes, which have Doppler velocities less than ±50 m/s with narrow spectral widths of <20 m/s (Grocott et al., 2013; Nishitani et al., 2011), or in the ionospheric scatter echoes, typically with Doppler velocities greater than ±50 m/s and wide spectral widths of >50 m/s (Grocott et al., 2013; Ponomarenko et al., 2009).

SuperDARN may observe *E*-region coherent echoes at ∼95–125 km altitude in the first few near range gates (0–3), typically 180–315 km downrange due to its oblique sounding, called Near Range Echoes (NREs) (Hall et al., 1997; Hussey et al., 2000; Jenkins & Jarvis, 1999; Ogawa et al., 2009). These may have several sources. Intermittent meteor trails at ∼80–120 km altitude cause NREs (Hall et al., 1997; Hussey et al., 2000; Jenkins & Jarvis, 1999). NREs have been associated with Polar Mesospheric Summer Echoes (PMSEs) at ∼80–85 km altitude (e.g., Hosokawa et al., 2005; Ogunjobi et al., 2015, 2017). However, there is some doubt about this mechanism based on altitude observations (Ponomarenko et al., 2016) and because NREs are also observed in the winter. The Polar Mesospheric Winter Echoes (PMWEs) phenomenon only occurs sporadically at ∼50–85 km altitude (Kavanagh et al., 2006), which corresponds to SuperDARN ranges less than the typical minimum (180 km). Another type of NRE is the High-Aspect Angle Irregularity Regions (HAIR), which is related to the Farley-Buneman Instability (FBI) at an altitude of ∼120 km for higher ionospheric electric fields (>40 mV/m) (Drexler & St-Maurice, 2005; St.-Maurice & Nishitani, 2020) and so-named because ray path orthogonality is not strictly required.

In addition, St.-Maurice and Nishitani (2020) found that SuperDARN NREs are associated with the Gradient Drift Instability (GDI) at an altitude of ∼100 ± 3 km. These radar echoes were named Far-Aspect Angle Irregularity Regions (FAIR). GDI results from the presence of a plasma density gradient in a favorable direction to allow GDI growth, which is driven by the neutral wind ($\boldsymbol{U}_n$) and ion drift ($\mathbf{V}_i$) (Makarevich, 2014; Sojka et al., 1998; Y. Liu et al., 2019). In the ionosphere, GDI and NREs are closely linked with zonal neutral wind and ion drift (equivalently meridional ionospheric convection electric field ($\mathbf{E}_o$)) and plasma density gradients (∇n_e) (St.-Maurice & Nishitani, 2020), all of which occur routinely. If plasma convecting in the ionosphere encounters a change in plasma density (equivalently conductivity), then the ions flow faster/slower in the region of higher/lower conductivity. At the boundaries of the plasma irregularities, charges will build up because ions arrive faster than they can depart or vice versa. The electrons are relatively unaffected because of their much lower collision (ν) to gyration (Ω) frequency ratio. The charge imbalance at a plasma density boundary sets up a counter polarization electric field, which then exerts its own $\mathbf{E} \times \mathbf{B}$ force on the plasma. With the correct geometry, the boundaries of the plasma irregularities become reinforced (i.e., steeper plasma density gradients), thereby enhancing polarization electric field, thereby resulting in positive feedback and hence the GDI grows.

The SuperDARN backscatters associated with NREs are generated through a secondary process where the large-scale gradient drift waves, of the order of 100 m, trigger secondary Farley-Buneman waves of the order of 10 m (St.-Maurice & Nishitani, 2020; Tsunoda et al., 1994). This process occurs most efficiently at ∼98 km altitude (Tsunoda et al., 1994) and is the most efficient way in which the 10–15 m plasma structures observed by SuperDARN HF radars can be developed (St.-Maurice & Nishitani, 2020). Figure 1 demonstrates the GDI process that leads to the observed NREs for southern hemisphere geometry. At high latitudes in the lower *E*-region (∼100 km altitude), the ions are unmagnetized due to collisions with the neutrals (i.e., $\nu_{in} \gg \Omega_i$), so they tend to drift ($\mathbf{V}_\mathrm{i}$) in the electric field (**E**) direction, whereas the electrons are magnetized (i.e., $\nu_e \ll \Omega_{en}$), so they drift ($\boldsymbol{V}_e$) in the $\mathbf{E} \times \mathbf{B}$ direction. Panel (a) shows two regions with different plasma densities (n) such that $\mathrm{n}_1 > \mathrm{n}_2$. In the *E*-region,

$\mathbf{V_i}$ is approximately in the direction of $\mathbf{E}$ but the amplitude of $\mathbf{V_i}$ depends on the plasma density. Panel (b) shows that any random wave-like perturbation at the boundary will result in positive charges accumulating at a boundary due to more ions arriving than departing and vice versa. Alternating polarization electric fields ($\mathbf{E_p}$) are set up, creating $\mathbf{E_p} \times \mathbf{B}$ drifts ($\mathbf{V_d}$) as shown, which further enhance the boundary perturbation. Panel (c) shows the two different plasma regions that penetrate one another as the instability grows, which break down into narrow finger-like structures of shorter wavelength. Panel (d) shows that the finger-like structures of plasma density separate and substructures of plasma irregularities will be created in all directions perpendicular to the magnetic field (Gondarenko & Guzdar, 2001), which form a source of radar echoes when the Bragg scatter condition is met, that is, 10–15 m for SuperDARN radars (Greenwald et al., 1995; Ponomarenko & Waters, 2006). These substructures are effectively visible to radars from almost all directions (St.-Maurice & Nishitani, 2020) and therefore do not have to be magnetic field-aligned. We note that in the *F*-region, where both electrons and ions are fully magnetized, we require $\mathbf{E}$ quasi-parallel to ∇n_e (Y. Liu et al., 2019) so that $\mathbf{V_i}$ remains quasi-perpendicular to ∇n_e. This change in horizontal *E*-field direction gives the same geometry for GDI in the collision-less *F*-region as it does for the collisional *E*-region.

SuperDARN HF radars observe the FAIR echoes caused by the GDI cascading to shorter wavelengths (St.-Maurice & Nishitani, 2020). The GDIs are triggered when there is a strong enough plasma density gradient through which the ions must drift, which may happen during auroral precipitation or in the presence of sporadic *E*-layers (*Es* layers) (Kagan & Kelley, 1998; Kirkwood & Von Zahn, 1991). Sometimes, during geomagnetic storms and auroral precipitation, both the GDI at ∼100 km altitude (for FAIR echoes) and the FBI at ∼125 km altitude (for HAIR echoes) may occur simultaneously (St.-Maurice & Nishitani, 2020), potentially making clear identification of each echo type difficult.

There is a strong electric field coupling between the ionospheric *F* and *E* regions because the magnetic field is essentially equipotential and the distance is only a few 100 km (Farley Jr, 1960). Also, at high latitudes, the magnetic field is near-vertical allowing for near-coincidence of *E* and *F* region phenomena in the horizontal direction. Numerous studies, mainly at midlatitudes, have shown electric field coupling between the *E* and *F* regions of the ionosphere involving TIDs (e.g., Haldoupis et al., 2003; Kotake et al., 2007; Otsuka et al., 2004, 2007, 2009; Tsunoda & Cosgrove, 2001; Y. Liu et al., 2019; Zhou et al., 2018). In addition, multiple midlatitude studies have shown that TIDs occur simultaneously with sporadic *E*-layers in the majority of cases (e.g., Tsunoda & Cosgrove, 2001 and references therein).

In this paper, we show for the first time the effects of MSTIDs, observed by southern hemisphere SuperDARN HF radars in the *F*-region ionosphere far ranges, on NREs observed by the same radars in the *E*-region near ranges with a suitable time delay determined by the MSTID velocity vector and assuming a constant propagation altitude. Furthermore, we show that the phenomenon is consistent with the MSTID, partially modulating the GDI mechanism.

2. Theory of *E*-Region Instabilities

Two kinds of ionospheric plasma instabilities that may lead to SuperDARN backscatter are possible: the first one is FBI or the related Two-Stream Instability (TSI) (Kelley, 2009; Keskinen & Ossakow, 1983). The second one is the GDI (St.-Maurice, 1985; St.-Maurice & Nishitani, 2020). The plasma oscillation frequency (ω_r) and growth rate (γ) from the local linear theory of GDI and FBI/TSI in the reference frame of the neutral wind are given by Kagan and Kelley (1998), Kelley (2009), and Kelly (2012):

$$\omega_r = \frac{\mathbf{k}.(\mathbf{V_i} + \boldsymbol{\psi}\mathbf{V_i})}{1 + \boldsymbol{\psi}}$$

and

$$\gamma = \frac{1}{1+\boldsymbol{\psi}}\left[\left(\frac{\boldsymbol{\psi}}{\nu_i}\right)\left[(\omega_r - \mathbf{k}.\mathbf{V_i})^2 - k^2 C_s^2\right] + \left(\frac{1}{Lk^2}\right)(\omega_r - \mathbf{k}.\mathbf{V_i}) + \left(\frac{\nu_i}{\Omega_i}\right)k_y\right] - 2\alpha n_0 \qquad (1)$$

where

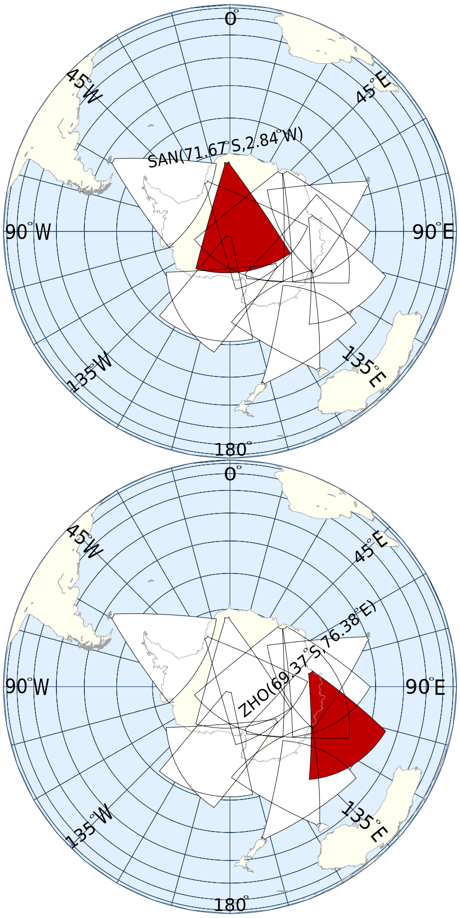

Figure 2. Southern hemisphere SuperDARN HF radars' fields of view. SANAE (top) and Zhongshan (bottom) radars' fields of view are shown in red.

$$\psi = \psi_o \left[\left(\frac{k_\perp^2}{k^2} \right) + \left(\frac{\Omega_e^2}{\nu_e^2} \right) \left(\frac{k_\parallel^2}{k^2} \right) \right].$$

and **k** is the wavenumber of plasma wave, C_s is the ion-acoustic velocity, $\mathbf{V_i} = (\mathbf{E} \times \mathbf{B})/B^2$ is the ion drift velocity, L is the plasma density (n_e) gradient scale length ($L_z = 1/(\partial ln(n_e)/\partial z)$) (St.-Maurice & Nishitani, 2020), ν is the collision frequency, and Ω is the gyrofrequency. The first term with the diffusive damping $\left(k^2 C_s^2\right)$ describes the FBI or TSI, while the second term with L describes the GDI. The third term $(\nu_i/\Omega_i)k_y$ describes the recombination damping. We neglect FBI/TSI because it is only valid for short wavelengths (i.e., $L \Rightarrow \infty$) (Kelley, 2009; Keskinen & Ossakow, 1983), and also it requires a strong electric field of at least ∼40 mV/m to occur (St.-Maurice, 1985). The linearized growth rate for GDI (γ) can then be written as (Woodman et al., 1991):

$$\gamma \propto \frac{1}{1+\psi} \mathbf{k}.\mathbf{V_i} \left(\mathbf{k}.\nabla n_e \times \mathbf{B} \right) \tag{2}$$

For GDI to grow in the E-region, a significant component of $\mathbf{V_i}$, ∇n_e, and **B** must be mutually perpendicular (Fejer et al., 1984; Y. Liu et al., 2019) as indicated in Figure 1. The gradient scale length in the vertical direction (L_z) is estimated by rearranging Equation 7 of St.-Maurice and Nishitani (2020). The lowest threshold condition to trigger the GDI that is responsible for the FAIR echoes, which are observed as NREs by SuperDARN, is given by:

$$L_z = \frac{(U_{nx} + E_y/B)\,\Omega_e \cos D}{(1+\psi_o)\,(k_x.C_s)^2 \left(\frac{\nu_{en}}{\nu_{in}} \right)} \tag{3}$$

where $\psi_o = \frac{\nu_{en}\nu_{in}}{\Omega_e \Omega_i}$ and $k_x = k \cos\beta \sin\theta$ and where U_{nx} is the geographic zonal neutral wind, β is the aspect angle between **E** and **k**, and θ is the flow angle between $\mathbf{V_i}$ and **k**. The smaller the value of L_z, the greater the growth rate (γ) of the GDI. Control of L_z is by the term ($U_{nx} + E_y/B$), that is, the relative wind and ion drift velocities, and minimizes when the wind opposes the ion drift with similar velocity. Normally, the ion drift speed (E_y/B) is greater than the neutral wind (U_{nx}), so the ionospheric electric field is the primary controlling term for the GDI growth rate. L_z has been measured in the high-latitude E-region (Haldoupis et al., 2000). They found that $L_z \approx$ 4–7 km around ∼100 km altitude, the minimum value being limited by the 3 km radar range resolution. Such small structures should trigger the GDI for a modest ionospheric electric field (St.-Maurice & Nishitani, 2020). Unsurprisingly, Haldoupis et al. (2000) found that L_z takes on larger values at higher altitudes in the topside ionosphere, that is, from 10 km to greater than 25 km.

Normally, GDI growth relates to the plasma density gradient component perpendicular to the magnetic field (L_x) as shown in Figure 1. At high latitudes, the magnetic field is near-vertical. In order to get the appropriate value of L_x, the magnetic dip angle (I) must be taken into account (Haldoupis et al., 2000):

$$L_x = \frac{L_z}{\cos(I)} \tag{4}$$

3. Instruments and Models

The SuperDARN HF radar network (Chisham et al., 2007; Greenwald et al., 1995) is used collectively to estimate the ionospheric electric field **E** and polar cap electrostatic potential using the ionospheric plasma drift $\mathbf{V_i} = \mathbf{E} \times \mathbf{B}$ Doppler observations in the plane perpendicular to the magnetic field **B** and fitting to a spherical harmonic model (Chisham et al., 2007; Fiori et al., 2013; Shepherd & Ruohoniemi, 2000). Figure 2 shows the 13 southern hemisphere SuperDARN radars' fields of view (FOV) with the South African SANAE and Chinese Zhongshan radars shown in red. SANAE is located at 71.67°S, 2.84°W (66.64°S, 48.51°E geomagnetic coordinates) and Zhongshan is located at 69.38°S, 76.38°E (74.5°S, 96.0°E geomagnetic coordinates). For SANAE, LT = UT + 2 hr and MLT ≈ UT − 2 hr. For Zhongshan, LT = UT + 5 hr and MLT ≈ UT + 2 hr. The SANAE and Zhongshan radars' geographic boresight directions are 173.2° and 72.5°, that is, approximately southward and eastward, respectively. Both radars have 16 beams covering ~53° azimuth with a range resolution of 45 km and the first gate at 180 km downrange. The SANAE beams are numbered from zero anticlockwise, while Zhongshan is clockwise in azimuth angle. SANAE and Zhongshan operated continuously on 12.57 and 10.25 MHz, respectively, with a 2-min temporal resolution during this study. All SuperDARN HF radars provide backscatter power, line of sight Doppler velocity, and spectral width data products (Chisham et al., 2007). For this study, these data are estimated by fitting the autocorrelation function (Baker et al., 1995; Ponomarenko et al., 2009) using FITACF Version 2.5, obtained through the radar software toolkit Version 4.3.

To obtain the magnetic field, we use 1-min magnetometer data from SANAE (Kotzé, 2018) and Zhongshan (Y. Liu et al., 2016). Magnetic field data were used to calculate the electron and ion gyrofrequencies. To check for the existence of *Es* layers, we use the Digisonde Portable Sounder 4D located at Zhongshan with an hourly time resolution (Li et al., 2007). No ionosonde was available close to SANAE.

The International Reference Ionosphere (IRI) 2016 model (Bilitza et al., 2017) was used to obtain electron density and temperature. The Mass Spectrometer, Incoherent Scatter (MSIS)-E-90 atmospheric model (Hedin, 1988), was used to obtain neutral particle number densities and temperature profile in the thermosphere. Both models are used to determine the ionospheric Pedersen conductance and particle collision frequencies. The 2014 Horizontal Wind Model (HWM14; Drob et al., 2015) was used in this study because observations of upper atmospheric neutral winds were not available.

4. Observations

We present 3 representative data sets, out of more than 175 found in the southern hemisphere SuperDARN data from 2010 to 2013, that showed MSTIDs partially modulating NREs in the same radar data set. The original cause of the MSTIDs is beyond the scope of this paper. Our focus is on the interaction of the observed MSTIDs on existing NREs. A statistical survey of the 175 cases found so far will form a future study. Obviously, since TIDs are typically observed in the *F*-region far ranges and NREs are only observed in the *E*-region near ranges, their coincidence is only near-simultaneous, the timing offset depending on the speed and direction of the MSTID. One event occurred during winter on 15 July 2012 over noon at SANAE, and the other two occurred in summer on 22 November and 17 December 2013 post-midnight and pre-midnight, respectively, at Zhongshan. The high latitude, season, and time of the observations mean that the sun was at low elevation for Zhongshan and well below the horizon for SANAE, that is, solar illumination would have been weak. We choose these data sets because they provide a variety of seasons and local times. The SANAE radar FOV is essentially poleward and covers both the auroral oval as well as the polar cap (see Figure 2). The Zhongshan radar FOV is essentially eastward with the facility under the magnetospheric cusp region at noon and under the polar cap region during the night (Li et al., 2007).

Figure 3 shows the range-time-intensity plots for the three selected data sets. Backscatter power (dB) is shown in pseudo-color for beam 15 in all cases. The TIDs are highlighted by slanted solid lines for visual reference only and the NREs are shown in a solid rectangle. We assume the TIDs propagated at a constant altitude and velocity (cf., He et al., 2004; Grocott et al., 2013); hence, the straight lines overlaid. Panel (a) shows SANAE data for 11:00 to 17:00 UT on 15 July 2012, corresponding to ~09:00–15:00 MLT with $Kp = 5^{+} - 6$ indicating high geomagnetic activity. Between 12:00 and 17:00 UT, periodic backscatters are clearly observed for slant ranges ~1,100–2,600 km, indicating TIDs propagating away from the radar. Line-of-sight Doppler velocities and spectral widths (shown in Appendix A by Figure A1) were up to 1,000 m/s away from the radar and up to 125 m/s, respectively. Panel (b) is similar to panel (a) but for 00:00 and 04:00 UT on 22 November 2013 for the Zhongshan HF radar, corresponding to ~02:00–06:00 MLT, with $Kp = 1^{-} - 0$, indicating quiet geomagnetic conditions. The TIDs propagated toward the radar between 00:00 and 04:00 UT at a slant range of ~350–1,700 km. Line-of-sight Doppler velocities and spectral widths (shown in Appendix A by Figure A1) were up to 400 m/s toward the radar and mostly less than 12 m/s, respectively. Panel (c) is similar to panel (b) but for 17:00–22:00 UT on 17 December 2013 for the Zhongshan radar, corresponding to ~19:00–24:00 MLT, with $Kp = 1^{-} - 2^{+}$, indicating

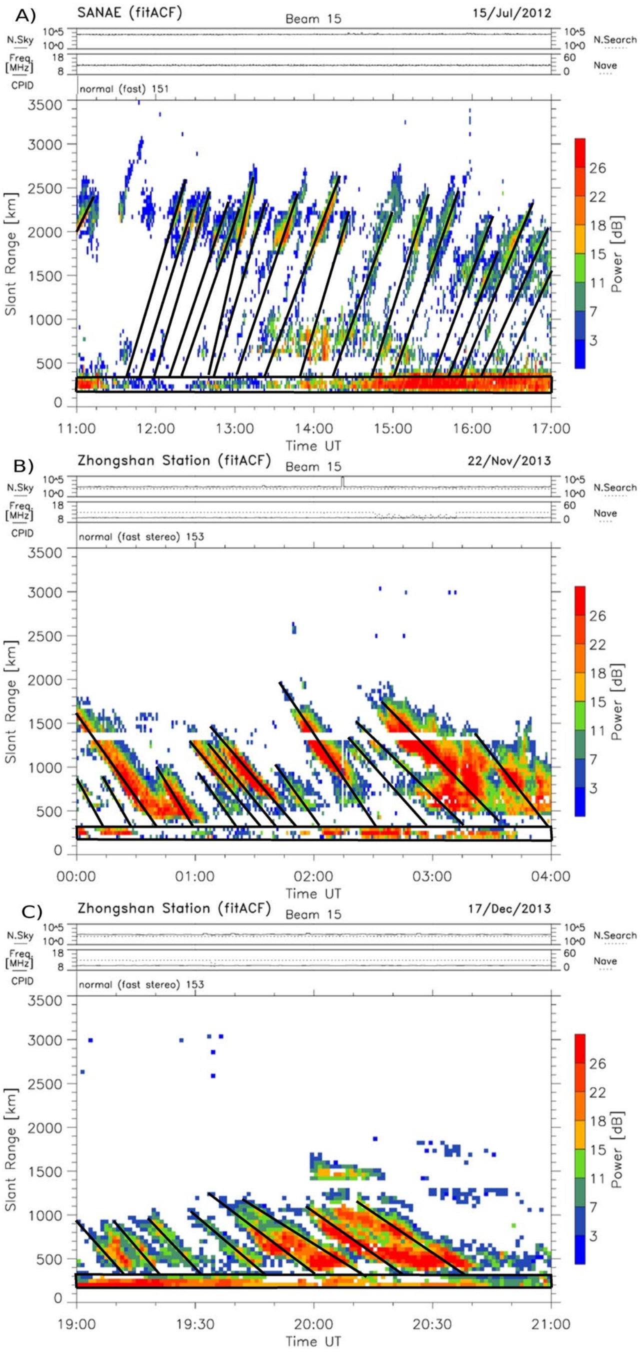

Figure 3. Range-Time-Intensity plot of backscatter power of (a) beam 15 of the SANAE HF radar from 11:00 to 17:00 UT on 15 July 2012, (b) beam 15 of the Zhongshan HF radar from 00:00 to 04:00 UT on 22 November 2013, and (c) beam 15 of the Zhongshan HF radar from 19:00 to 21:00 UT on 17 December 2013. The slant black lines approximately indicate wavefronts of Traveling Ionospheric Disturbances. The horizontal black rectangles show the Near Range Echoes.

low geomagnetic activity. Between 19:00 and 21:00 UT, the TIDs propagated toward the radar at a slant range of ~350–1,250 km. Line-of-sight Doppler velocities and spectral widths (shown in Appendix A by Figure A1) were up to 400 m/s toward the radar and mostly less than 12 m/s, respectively. The true vector velocity of the TIDs was obtained using the multi-beam method described by He et al. (2004) as discussed below. For the sake of brevity, we name the events observed on 15 July 2012, 22 November 2013, and 17 December 2013 as S1, Z1, and Z2, respectively.

In all cases, the SuperDARN ray tracing (shown in Appendix A by Figure A2) showed that the backscatter was ionospheric. Based on possible magnetic field orthogonal backscatter from the ray tracing, the TIDs propagated at ~400, ~300, and ~240 km altitude for cases S1, Z1, and Z2, respectively. *F*-region ionospheric propagation is consistent with the high TID Doppler velocities and high spectral width for case S1. Cases Z1 and Z2 are mostly at ranges too short to allow for ground scatter. Simultaneously, for all cases, NREs are observed between a slant range of 180 and 315 km. However, a clear one-to-one correspondence between the TID and NRE backscatter power is not immediately obvious by visual inspection. A visual comparison is also made difficult because of naturally occurring data gaps in the NREs and the lack of far range backscatter does not necessarily imply that MSTIDs were not present.

Figure 4 shows the SuperDARN map potential plots for cases S1, Z1, and Z2 with the vectors of plasma convection flow observed by the southern hemisphere radars. Overlaid are particle precipitation data showing the logarithm of electron energy flux between 0 and 30 kev cm^{-2} s^{-1} sr^{-1} from the TED instrument of the POES satellites (cf., Atilaw et al., 2021) and the estimated equatorward boundary of the auroral oval (red dotted-dashed circle). The approximate FOV of the relevant radar is shown overlaid. Panels (a–c) correspond to cases S1, Z1, and Z2, respectively. Figure 4 illustrates that the TID-modulated NREs occur at times when the radars' FOVs were within the auroral oval, and the associated particle precipitation (highlighted by the POES TED data) would have created *E*-region plasma density perturbations in the radar near ranges, thereby creating conditions favorable to the formation of GDI. We note that the NREs for case S1 were initially in the dawn convection cell and later in the dusk cell. For case Z1, the NREs appear only in the dawn convection cell. For case Z2, the NREs appear initially in the dusk convection cell and then later the dawn cell.

For case Z2, we were able to reinforce the expectation that plasma density gradients existed by local ionosonde observations. Figure 5 shows two example ionograms observed from Zhongshan at 19:00 and 21:00 UT on 17 December 2013. Spread-*F* is visible above 250 km, consistent with particle precipitation, and an *Es* layer appeared from 18:00 to 22:00 UT at ~100 km altitude, varying between 95 and 118 km. The appearance of an *Es* layer is consistent with Tsunoda and Cosgrove (2001) who noted that TIDs and *Es* layers occur simultaneous in the majority of cases. A sporadic *E*-layer provides a suitable plasma density gradient required for the GDI to exist (Kagan & Kelley, 1998; Kirkwood & Von Zahn, 1991). Unfortunately, no ionosonde data are available for cases S1 and Z1. Of the 175 similar TID-NRE events identified over Zhongshan, 153 had ionosonde data and of those 84% had a simultaneous *Es* layer present. Of these, 47% occurred in winter and 53% occurred in summer. This coincidence between TIDs and Es layers is similar to that found by Goodwin (1966) (75%) and Bowman (1960, 1968) (85%).

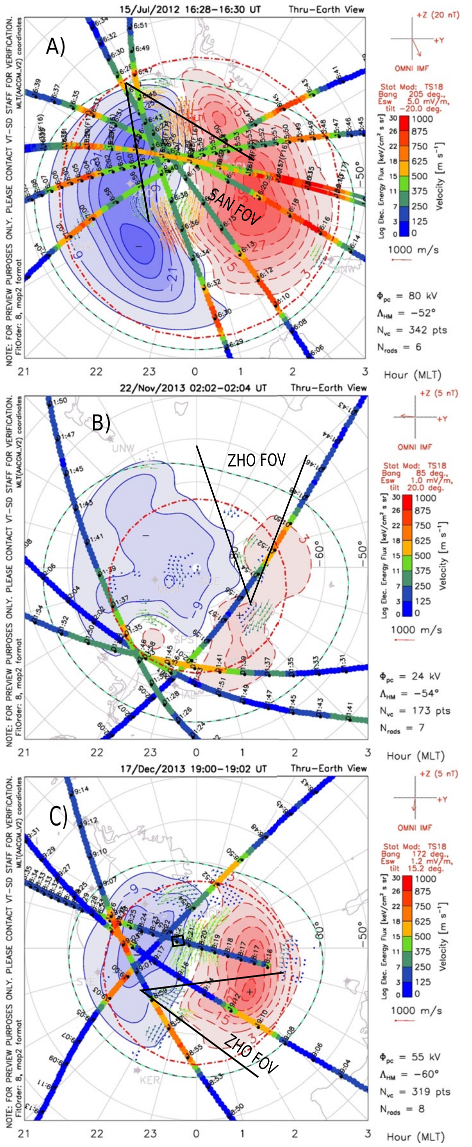

Figure 4. SuperDARN map potential plot (using FITACF V2.5) showing the vectors of convection plasma flow derived from the southern hemisphere radars overlaid on a MLT-MLAT grid along with particle precipitation data from the TED instrument of the POES satellites. Panels (a–c) are for cases S1 (15 July 2012, winter), Z1 (22 November 2013, summer), and Z2 (17 December 2013, summer), respectively. The estimated equatorward edge of the auroral oval boundary is shown by the red dotted-dashed circle. The approximate fields of view of the relevant radar is shown overlaid.

5. Characteristics of MSTIDs

We have estimated the TID parameters in the *F*-region ionosphere from the HF radar data using the fast Fourier transform (FFT) cross-spectral analysis algorithm described by He et al. (2004). For each radars' FOV, multiple sets of three range gates were used to estimate the wavenumber (k_x & k_y), phase velocity (v), wavelength (λ), propagation azimuth angle (Az) (e.g., Atilaw et al., 2021; Grocott et al., 2013), and amplitude (A) of the TIDs (cf., Francis, 1974; Hayashi et al., 2010). The near range gates, which contain the NREs studied here, were not used in this process. The TIDs periods were estimated using the FFT (He et al., 2004). From the peaks of the FFT spectrum, Table 1 shows the results of this analysis for each case. For case S1, the TIDs propagated with an average velocity of ∼308 m/s and a period of ∼28 min at a geographic azimuth angle of ∼197° with an amplitude of ∼82 km. For case Z1, the TIDs propagated with an average velocity of ∼431 m/s and a period of ∼15 min at a geographic azimuth angle of ∼222° with an amplitude of ∼60 km. For case Z2, TIDs propagated with an average velocity of ∼328 m/s and a period of ∼20 min at a geographic azimuth angle of ∼298° with an amplitude of 63 km (see Supporting Information S1). The observations clearly fit the definition of MSTIDs (Grocott et al., 2013; He et al., 2004). In addition, MSTID amplitudes are consistent with high-latitude incoherent scatter radar observations (Senior et al., 2006).

To demonstrate a definite link between the observed MSTIDs and NREs, we have performed an FFT analysis (shown in Appendix A by Figures A3, A4 and A5 for cases S1, Z1, and Z2, respectively) on the two different echo types at both near and far ranges. For this analysis, the SuperDARN data were resampled at 1-min resolution, corresponding to a Nyquist frequency resolution of 8.3 mHz. For both the NREs and MSTIDs, coinciding FFT peaks were found at ∼28, ∼15, and ∼20 min for case S1 (see Figure 3a and Figure A3), case Z1 (see Figure 3b and Figure A4), and case Z2 (see Figure 3c and Figure A5), respectively (see Table 1), corresponding to the backscatter periods visible in Figure 3.

6. Cross Correlation Between MSTIDs and NREs

To further establish the link between MSTIDs and NREs, we have performed a cross-correlation analysis on the two different echo types (shown in Appendix A by Figure A6). For case S1 with beam 15 and range gate 2 (270 km, NREs) against range gates 40–45 (1,980–2,205 km, TIDs), the cross-correlation coefficient (CC) peaks at ∼0.5 with a time lag of ∼45 min. For case Z1 with beam 15 and range gate 1 (225 km, NREs) against range gates 19–24 (1,035–1,260 km, TIDs), the correlation coefficient peaks at ∼0.53 with a time lag of ∼25 min. For case Z2 for beam 15 and range gate 1 (225 km, NREs) against range gates 10–15 (630–855 km, TIDs), the correlation coefficient peaks at ∼0.55 with a time lag of ∼9 min. In all cases, the cross-correlation time lag is consistent with the expected propagation delay of the MSTIDs observed (see Figure 3 and Table 1). We note that the cross correlation is moderate in all cases but this is consistent the observed NREs, which show little obvious sign of modulation by the MSTIDs (see Figure 3). As noted above, visual detection of TID modulation in the NREs is made difficult partly because of naturally occurring backscatter variability and data gaps in the NREs. In addition, data gaps in the far range backscatter do not necessarily imply that MSTIDs were not present. We have performed an FFT analysis in the NREs before and after the times of the observed MSTIDs for the events presented here and found no evidence of MSTID periods in the NRE backscatter (see Supporting Information S1).

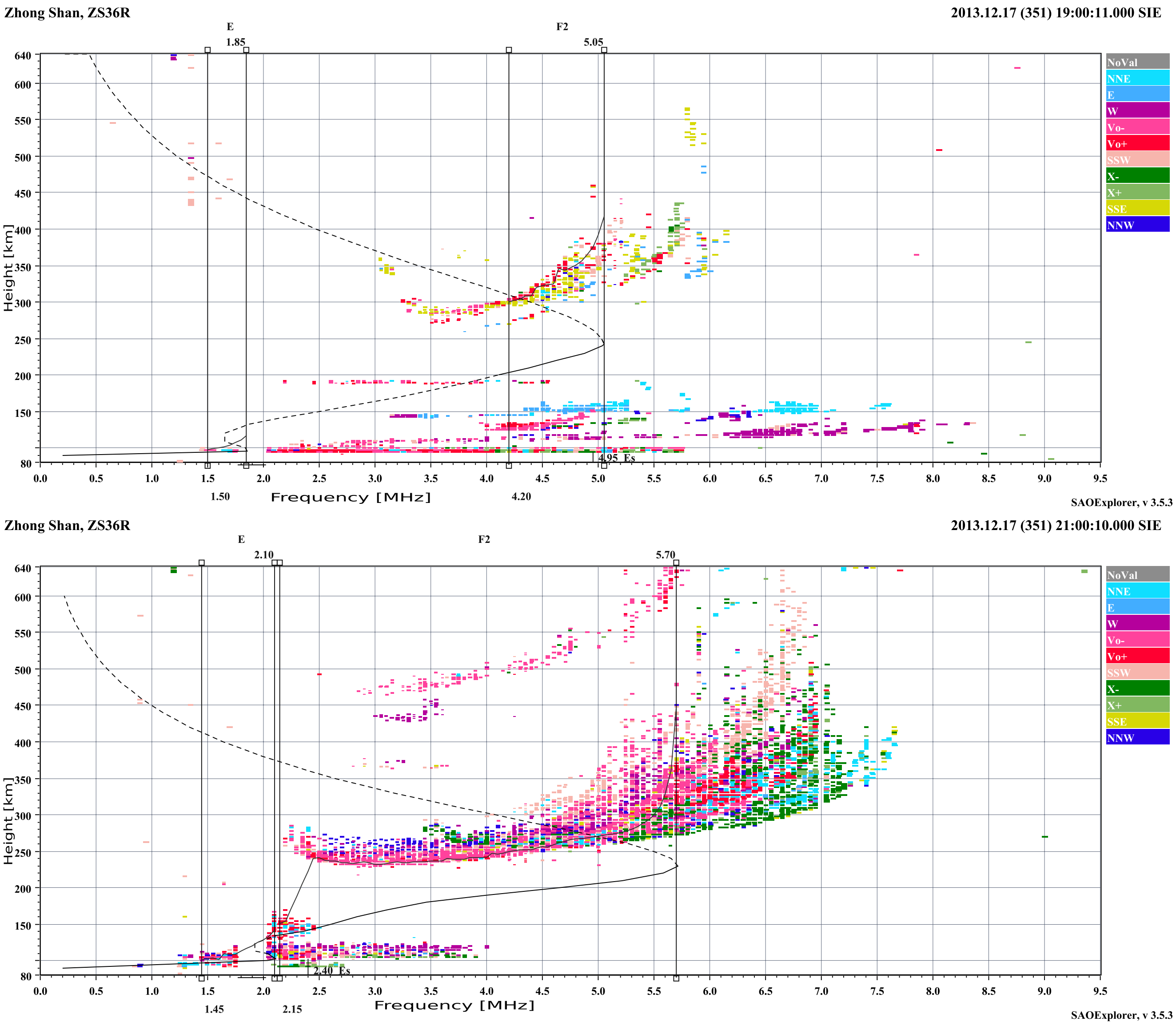

Figure 5. Hourly ionograms from Zhongshan at 19:00 and 21:00 UT on 17 December 2013 (case Z2).

Clearly, the amplitude modulation of the NREs shown in Figure 3 is not immediately obvious as it is for the MSTIDs. This is reflected in the moderate cross-correlation values described above. Here, we focus the analysis on gates 1 and 2 for all beams, neglecting gates 0 and 3 although they do show evidence of NREs. First, gates 1 and 2 have fewer data gaps. Second, SuperDARN radars sound obliquely, so each range gate is at a different altitude. We do not have angle-of-arrival data available. However, St.-Maurice and Nishitani (2020) showed (see their Figure 2, bottom panel) that FAIR echoes at high latitude were observed at ~25–27° elevation angle, whereas in their case, HAIR echoes were observed at longer ranges and lower elevation angles. Our gates 1 and 2 best fit the criteria for observing FAIR echoes at ~100 km altitude. Using the Spearman rank correlation on gates 1 and 2 of all beams, we estimate the NRE amplitude modulation to be 8.9 (1.3)%, 8.1 (1.3)%, and 12.9 (1.4)% for cases S1, Z1, and Z2, respectively, where the values in brackets give the standard deviation. The impact of the MSTID passing overhead is ~10% of the NRE amplitude, which is consistent with the moderate cross-correlation values described above. This relatively modest amplitude modulation shows that the MSTIDs are having an effect on the NREs but that the fundamental causative mechanism for the NREs is not the MSTIDs themselves. This is obvious for cases Z1 and Z2 where the MSTIDs originated far away from the NREs and propagated toward the radar.

Table 1

Medium-Scale Traveling Ionospheric Disturbance (MSTID) Parameters Estimated on 15 July 2012 From 12:30 to 16:30 UT (Case S1), 22 November 2013 From 00:00 to 03:48 UT (Case Z1), and on 17 December 2013 From 19:00 to 20:48 UT (Case Z2)

Periods, wavenumbers, velocities, azimuth, wavelengths, and amplitudes of MSTIDs

Parameters	15 July 2012	22 November 2013	17 December 2013
T (min)	28	15	20
kx (/m)	11.2×10^{-6}	8.6×10^{-6}	11.3×10^{-6}
ky (/m)	4.9×10^{-6}	14.4×10^{-6}	11.3×10^{-6}
v (m/s)	308	431	328
Az (°)	197	222	298
λ (km)	514	375	393
A (km)	82	60	63

Note. Az is defined in geographic coordinates (see Figure 1).

7. Gradient Drift Instability in the *E*-Region

Next, we show that a link exists between the ionospheric electric field as determined by the SuperDARN network of radars and the NREs backscatter power. This provides a clue that GDI, which relies on the velocity difference between the ions and the slowly varying neutral wind (see theory section above), is a plausible mechanism for TID modulation of SuperDARN NREs. GDI requires plasma gradients (see theory section above) and we assume that these exist with the correct geometry (see Figure 1) because of the observed particle precipitation (see Figure 4) and for the one case where ionosonde data were available, a sporadic E-layer (see Figure 5). SuperDARN map potential data have a 2 min cadence with a 2° latitude and 1° longitude geomagnetic spatial resolution. The electric field was obtained by averaging the SuperDARN data from a selection of grid points closest to the observed NREs in time and position. Obviously, since all SuperDARN radars in both hemispheres contribute to the map potential data product, the contribution of an individual TID in any particular radar will be diluted. However, in our events (see Figure 3), there is significant ionospheric backscatter at range gates close to the NREs, especially for cases Z1 and Z2, which increases our confidence in the electric field estimate over the NREs.

We also estimate L_z from Equation 3 based on the ionospheric F-region electric field, taken from the SuperDARN radar network observations of ionospheric backscatter, the magnetic field and its dip angle, taken from local magnetometer data, and the E-region neutral wind, taken from the HWM14 wind model. We use IRI-2016 and MSIS-90 to estimate the ion-neutral and electron-neutral collision frequencies. We assume that the ionospheric electric field is unchanged in the E-region, given the relatively short quasi-vertical distance. The value of k_x (Equation 3) corresponds to the operating frequency of the SuperDARN radar, for example, for SANAE at 12.57 MHz, $\lambda = 2\pi/k_x \approx 12$ m. Equation 3 shows that when the relative ion-neutral velocity is large/small, then L_z becomes large/small resulting in a GDI growth rate (Equation 2), which is small/large, respectively. Therefore, a large relative velocity favors the production of NREs from GDI (St.-Maurice & Nishitani, 2020).

Assuming an ion-acoustic velocity $C_s \approx 300$ m/s (St.-Maurice & Nishitani, 2020), the inputs and outputs of Equation 3 are shown in Figure 6 for case S1 (15 July 2012) at 100 km altitude between 12:30 and 16:30 UT. We focus on 100 km altitude since FAIR echoes are believed to be triggered at near this altitude (St.-Maurice & Nishitani, 2020). Panel (a) shows the HWM14 model zonal neutral wind speed (U_{nx}), which varied smoothly between −5.4 and 14.8 m/s and reversed direction around 14:00 UT. Panel (b) shows the Z-component of the magnetic field **B** at SANAE. Panel (c) shows the meridional component of the ionospheric electric field (E_y) averaged over the closest magnetic coordinate to all beams for range gate 2. The electric field varies between 3 mV/m and −22 mV/m, which corresponds to an ion drift velocity of up to ∼−575 m/s. Hence, as expected, the neutral wind speed plays a minor role in Equation 3 for this case. Panel (d) shows the plasma density scale length (L_z), which varies from 370 to −2,592 m. The negative value for L_z indicates that the ion flow opposed the neutral wind with a greater velocity caused by the southward (negative) electric field. Unsurprisingly, given the small neutral wind, the variation in the meridional electric field is very similar to that in L_z. Panel (e) shows the backscatter power of gate 2 (p2), averaged over all 16 beams, received by the SANAE SuperDARN HF radar as NREs. The average backscatter power appears anticorrelated to E_y (panel c) and L_z (panel b). Panel (f) shows the cross correlation between E_y (panel c) and p2 (panel e) with a peak value of ∼-0.84 at zero lag. Panel (g) shows the cross correlation between L_z (panel d) and p2 (panel e) with a peak value of ∼−0.85 at zero lag. This clearly shows that the NRE backscatter power is closely related to the ionospheric convection electric field and therefore to the GDI mechanism. However, this does not (yet) take fully into account the additional effects of the MSTIDs on the NREs, which is discussed below. Since the MSTIDs modulate only ∼10% of the NRE backscatter power, it is expected that GDI-generated NRE be controlled primarily by the ionospheric convection electric field as shown here. Hence, the GDI-induced NREs would have existed without the presence of MSTIDs.

For case Z1 (shown in Appendix A by Figure A7), U_{nx} varied smoothly between 33.9 and 41.9 m/s, E_y varied between 1 and −24 mV/m, and L_z varied between −56 and −662 m. For case Z2 (shown in Appendix A by Figure A8), U_{nx} varied smoothly between 27.5 and 29.3 m/s, E_y varied between 3 mV/m and −6 mV/m, and

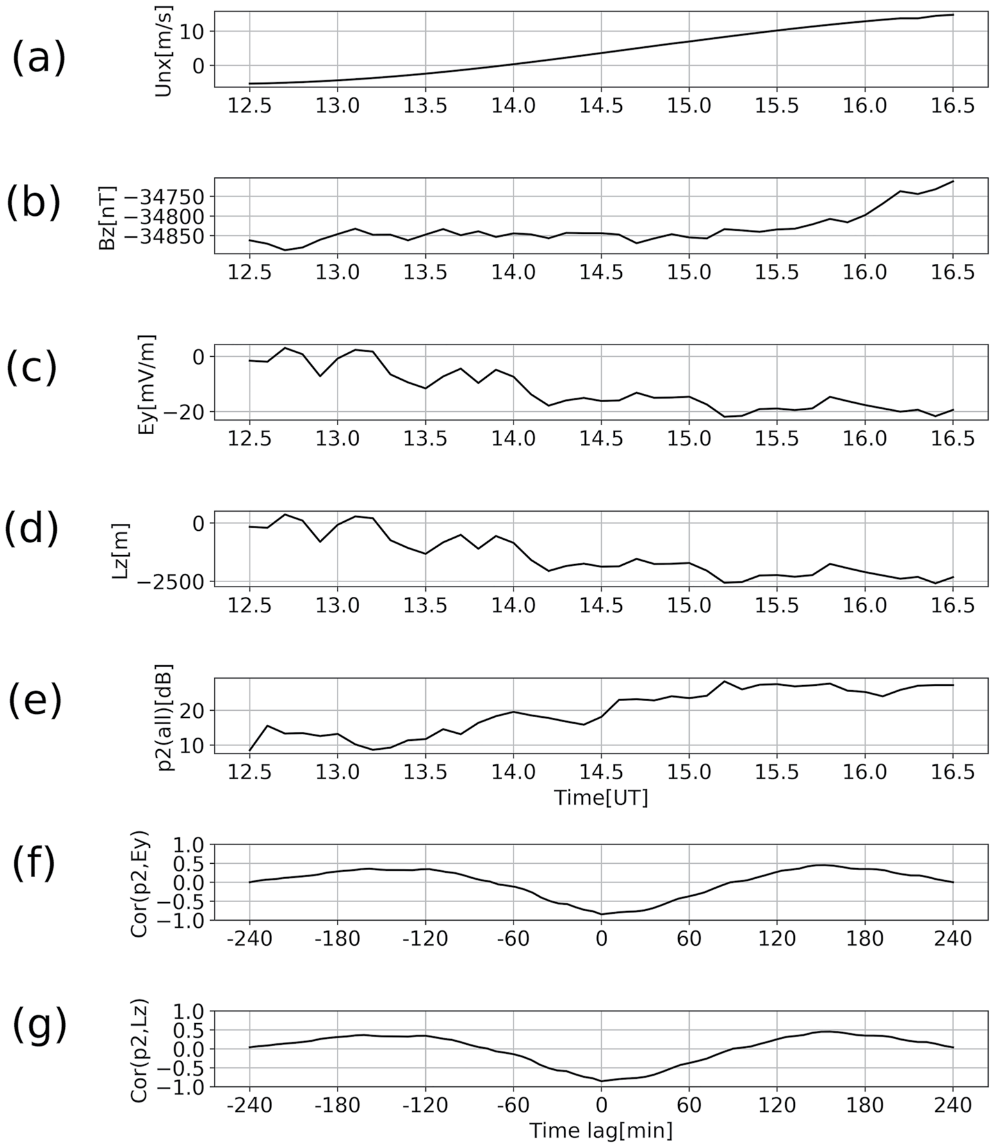

Figure 6. For 15 July 2012 from 12:30 to 16:30 UT at 100 km altitude (case S1), (a) modeled eastward neutral wind, (b) Z-component of the Earth's magnetic field at ground level, (c) observed northward electric field (E_y), (d) calculated plasma density scale height (L_z), (e) the average backscatter power of all beams for range gate 2 (p2), (f) the cross correlation between E_y (panel c) and p2 (panel e), and (g) cross correlation between L_z (panel d) and p2 (panel e).

Table 2
Cross-Correlation Coefficient (CC) Between the Average Power (p) of All Beams for Range Gates 1 and 2 and Either the Meridional Electric Field (E_y) or the Density Gradient Scale Height (L_z)

Date	15 July 2012	15 July 2012	22 November 2013	22 November 2013	17 December 2013	17 December 2013
CC of	*p* and E_y	*p* and L_z	*p* and E_y	*p* and L_z	*p* and E_y	*p* and L_z
Gate 1	−0.80	−0.81	−0.80	−0.80	−0.66	−0.66
Gate 2	−0.84	−0.85	−0.73	−0.74	−0.72	−0.72

L_z varied between 33 and −180 m. As Figure 1 shows, we require the GDI mechanism to operate perpendicular to the magnetic field in the *E*-region. We therefore need to map L_z to L_x using Equation 4 (Haldoupis et al., 2000). The magnetic dip angle at SANAE and Zhongshan is 61.7° and 73.2°, respectively. This means that $L_x = 2.1 \times L_z$ at SANAE and $L_x = 3.5 \times L_z$ at Zhongshan. Hence for cases S1, Z1, and Z2, $L_x \approx 777$ to $-5{,}443$, 196 to $-2{,}317$, and 116 to -630 m, respectively. These plasma gradient scale lengths are easily suitable for generating the GDI (cf., Haldoupis et al., 2000).

Table 2 shows the CC between the backscatter power of range gates 1 and 2 averaged over all 16 beams, and colocated ionospheric meridional electric field (E_y) as well as the plasma gradient scale height (L_z) for all cases. As explained above, we neglect gates 0 and 3 in this analysis. In all cases, there is a moderate (CC = −0.66) to strong (CC = −0.85) anticorrelation between E_y and L_z with the NRE backscatter power. This provides clear evidence that the GDI mechanism is operating for all our cases at the range gates that map most closely to ∼100 km altitude where FAIR echoes are expected (St.-Maurice & Nishitani, 2020).

8. FAIR Near Range Echoes

SuperDARN NREs in the *E*-region ionosphere may have multiple sources, such as short-lived meteor trails (e.g., Chisham & Freeman, 2013) and PMSEs (e.g., E. Liu et al., 2013; Hosokawa et al., 2005; Ogunjobi et al., 2017). We can exclude meteors because we observed NREs over many hours (see Figure 3). We can also exclude PMSE because we found events in the winter (e.g., case S1 on 15 July 2012 and 61 other winter NRE cases from 2010 to 2013) and PMWE generally occurs at lower altitudes below 85 km and therefore would not be visible in our radar data. Recent studies indicate that some of the NREs are from HAIR echoes (Ponomarenko et al., 2016; St.-Maurice & Nishitani, 2020) associated with the FBI. They require an electric field of >40 mV/m to be triggered at ∼120 km altitude, which corresponds to range gate numbers above 3 that are not observed in our events, and SuperDARN observations show that the electric field amplitude was always below 24 mV/m for our three events. FAIR echoes (St.-Maurice & Nishitani, 2020) are NREs believed to be associated with the GDI at ∼100 km altitude. These appear to be consistent with our observations for range gates 1 and 2.

We have established that particle precipitation existed in the vicinity of the SANAE and Zhongshan radar near ranges (see Figure 4) for all our events and on one occasion, a coincident sporadic *E*-layer was directly observed overhead (see Figure 5). Hence, suitable conditions existed in the *E*-region ionosphere for the GDI mechanism to produce FAIR echoes that then translated into the NREs observed by SuperDARN. We have observed MSTIDs propagating away/toward the radars and established that this backscatter occurred in the *F*-region. The observed NREs were partially modulated with the same period as the MSTIDs and with a time lag consistent with the MSTID propagation velocity in the *F*-region, assuming a constant altitude and velocity. The CC between MSTID backscatter and the NREs ranged from ∼0.50 to ∼0.55 for our events. We have performed an FFT analysis in the NREs before and after the times of the observed MSTIDs and found no evidence of MSTID periods in these NRE backscatters. When MSTIDs were present, we have estimated that the NRE amplitude modulation due to MSTIDs was in the range ∼8%–13%. We have estimated the CC between the ionospheric electric field and the NRE backscatter power, which was in the range of 0.66–0.84 for our events. We have estimated the CC between the ionospheric electric field and the plasma density scale length parameter (L_z), which controls the growth rate of the GDI mechanism, which was in the range from 0.66 to 0.85 for our events. Below we describe how an MSTID may partially modulate the existing GDI as we have observed in the NREs and estimate the amplitude of the GDI modulation from the MSTID parameters. This is then compared to the NRE amplitude modulation observed.

9. MSTID Polarization Electric Field

With reference to Figure 4, we note that for cases S1 and Z1, the MSTIDs had a southward component of the propagation direction, whereas the background ionospheric ion convection flow had a westward component of the drift direction. For case Z2, the MSTID had a westward component of propagation direction, whereas the background ionospheric convection flow had a northward component of drift direction. In all cases, the MSTID propagation direction and the ionospheric electric field ($\mathbf{E_o} = -\mathbf{V_i} \times \mathbf{B}$) had parallel components. This geometry is conductive for the GDI to occur, both for the generation of NREs due to the background ionospheric electric field and for the additional modulation of these NREs by the MSTID polarization electric field described below. The Pedersen current (**J**) in the *F*-region is given by (Kotake et al., 2007; Otsuka et al., 2007):

$$\mathbf{J} = \Sigma_p(\mathbf{E} + \mathbf{U} \times \mathbf{B}). \tag{5}$$

where Σ_p is the *F*-region Pedersen conductance. Hence, for our events, there will be a Pedersen current component parallel to the MSTID propagation direction. The MSTID wave perturbs the ionospheric plasma in the quasi-vertical field-aligned direction from which it follows that there will be an equivalent Pedersen conductance perturbation. In order to maintain divergence-free current continuity for **J**, a periodic horizontal polarization electric field ($\mathbf{Ep_F}$) must be set up locally within the MSTID wave. Figure 7 shows a cartoon depicting the geometry based on case S1 for the meridional projection. The MSTID propagates primarily southward in the

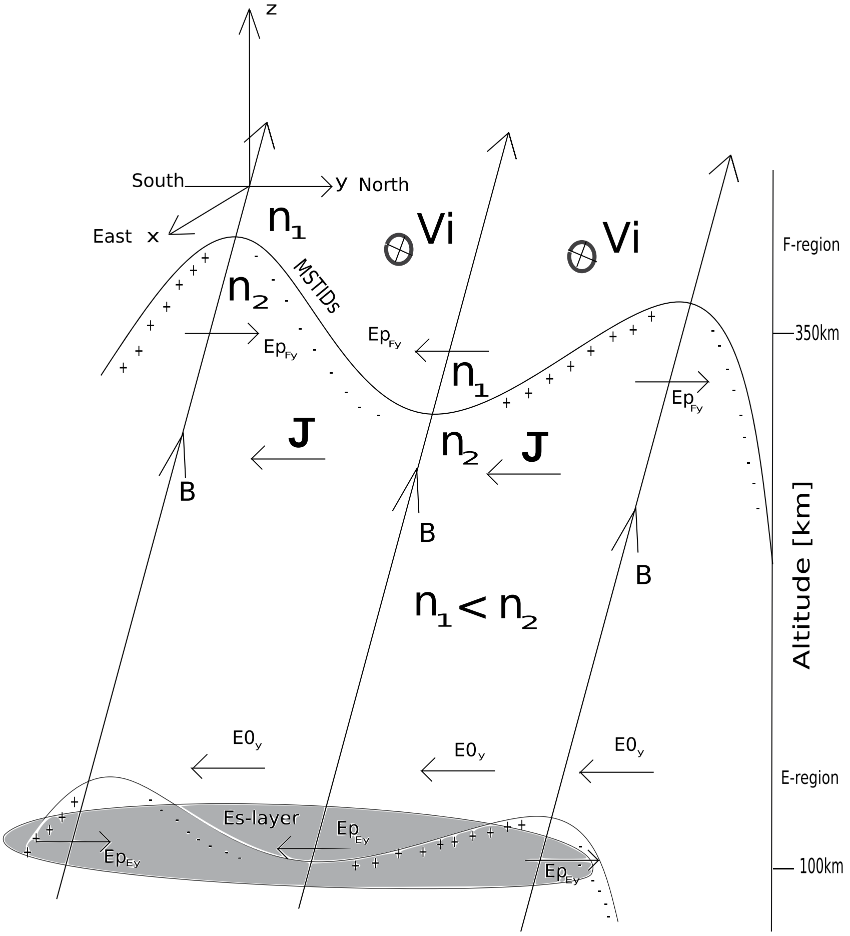

Figure 7. Cartoon showing how the polarization electric field due to a Medium-Scale Traveling Ionospheric Disturbance propagating in the *F*-region may partially modulate the existing Gradient Drift Instability in the *E*-region. The geometry is for the meridional projection of case S1 propagating above *hmF*2 in the southern hemisphere.

F-region, the ion drift is primarily westward and so the ionospheric electric field (**Eo**) and Pedersen current (**J**) are primarily southward. For case S1, the MSTID propagates at ~400 km (see Figure A2) above the *F*-region plasma density peak (~285 km), so the plasma density at higher altitude (n_1) is less than at lower altitude (n_2). In this case, positive/negative charges accumulate at the leading/trailing edge of the MSTID wave, resulting in an oscillating polarization electric field ($\mathbf{Ep_F}$) as shown. If the MSTID propagates below the *F*-region peak, then the plasma density gradient reverses, the position of the charges is reversed and the direction of $\mathbf{Ep_F}$ is also reversed. However, except for a phase shift, this does not change the mechanism. As the MSTID passes overhead in the *F*-region, it is the oscillating $\mathbf{Ep_F}$ that is transmitted undiminished downward along the equipotential magnetic field lines that partially modulate the background ionospheric electric field (**Eo**) in the *E*-region. Since the electric field ($\mathbf{Eo} + \mathbf{Ep_F}$) controls the growth rate of the GDI (see Equations 2 and 3), the NREs will be partially modulated spatially and temporally in a manner which mirrors the MSTID passing overhead. The forward motion of the MSTID ensures that steady-state saturation does not set in.

Finally, we show that the percentage amplitude modulation of **Eo** by $\mathbf{Ep_F}$ is consistent with the observed percentage modulation of the NREs (~8–13%). The polarization electric field shown in Figure 7 may be estimated as follows (Otsuka et al., 2007):

$$\mathbf{E}_{\mathbf{p_F}} = \frac{\delta\Sigma_p}{\Sigma_p}\left(\mathbf{E} + \mathbf{U}\times\mathbf{B}\right)\frac{\mathbf{k}}{|\mathbf{k}|} \tag{6}$$

where $\delta\Sigma_p$ is the change in *F*-region Pedersen conductance due to the MSTID, Σ_p is the unperturbed *F*-region Pedersen conductance, and **k** is the MSTID wavenumber vector. We used the MSIS and IRI models to compute the Pedersen conductance. We used the SuperDARN ray tracing tool to estimate the altitude of the MSTID propagation (see Figure A2 in Appendix A). The amplitude (A) of the MSTID wave is shown in Table 1. $\delta\Sigma_p$ is calculated by taking the difference between the height-integral of Pedersen conductivity above and below the MSTID propagation altitude, the height limits being set by the MSTID amplitude ($\pm A$). For case S1 with hmF2 = ~285 km, propagating at ~400 km altitude and $A = 82$ km, $\delta\Sigma_p/\Sigma_p = 9.9\%$. For case Z1 with hmF2 = ~255 km, propagating at ~300 km altitude and $A = 60$ km, $\delta\Sigma_p/\Sigma_p = 11.8\%$. For case Z2 with hmF2 = ~315 km, propagating at ~240 km altitude and $A = 63$ km, $\delta\Sigma_p/\Sigma_p = 16.6\%$. This level of *F*-region Pedersen conductance modulation is consistent with the ~10% airglow modulation by MSTIDs observed by Suzuki et al. (2009) at midlatitudes. We had estimated above the NRE amplitude modulation to be 8.9%, 8.1%, and 12.9% for cases S1, Z1, and Z2, respectively.

Hence, for cases S1/Z1/Z2, an ~9.9%/11.8%/16.6% modulation of **Eo** resulted in an NRE modulation of ~8.9%/8.1%/12.9%, respectively. We claim that in addition to the qualitative agreement shown above, this result provides quantitative agreement that the passing MSTIDs in the *F*-region, observed by the SuperDARN radars' far ranges, partially modulated **Eo**, which partially modulated the GDI, which partially modulated in equal measure the NREs observed by the same SuperDARN radars in the *E*-region. The MSTIDs are linked to the NREs by the quasi-vertical equipotential magnetic field lines.

10. Conclusions

In this work, we have shown the first near-simultaneous observations of MSTIDs partially modulating existing NREs observed by the SANAE and Zhongshan HF radars. Based on qualitative and quantitative analyses, we conclude that GDI is the most likely mechanism for MSTIDs propagating in the *F*-region to affect the NREs in the *E*-region. We summarize our results as follows:

1. High-latitude MSTIDs and NREs were observed during the noon and afternoon sectors during a geomagnetic storm in winter, and early morning and evening sectors during a geomagnetically quiet time in summer. The observed MSTIDs characteristics and the propagation directions were consistent with the previous studies. The GDI causes FAIR echoes in the lower *E*-region, which are observed as NREs in the SuperDARN data (St.-Maurice & Nishitani, 2020). The GDI occurs in pre-existing plasma density gradients (e.g., sporadic *E* (*Es*) layers), driven by the ionospheric meridional convection electric field and zonal thermospheric neutral winds.
2. Horizontally propagating MSTIDs generate an additional horizontal polarization electric field to conserve the divergence-free Pedersen current across the magnetic field. The meridional component of the net electric field (quasi-static convection plus oscillating TID polarization), mapped down from the *F*-region along the equipotential magnetic field lines (Sun et al., 2015; Y. Liu et al., 2019), partially modulates the existing GDI, which is responsible for generating the NREs in the lower *E*-region (St.-Maurice & Nishitani, 2020), resulting in the observed partial modulation of the NREs. For all radar gates analyzed in this study, the cross correlation between the meridional electric field or the plasma density gradient scale height and the backscatter power is between −0.66 and −0.85, indicating a good anticorrelation.
3. Most oblique sounding SuperDARN HF radars cannot estimate the altitude of the backscatter with high precision as vertical pointing VHF radars do and HF ray tracing contains uncertainties. There remains the problem of knowing without doubt if PMSEs are part of SuperDARN NREs (Ponomarenko et al., 2016). In principle, MSTIDs can modulate PMSEs in the same way AGWs modulate the Noctilucent Clouds (Dalin et al., 2004), but we are not sure if the phenomenon can be observed by SuperDARN HF radars. Our winter case (S1) seems to exclude PMWEs because they tend to occur at altitudes that correspond to ranges shorter than 180 km and therefore are generally not observed by the SuperDARN HF radars.

Appendix A: Additional Figures to Support Science of Three Cases Presented in the Main Text

The appendix contains additional important information to support the science case presented in the main text. Figure A1 shows the Doppler velocity and spectra width for Cases S1, Z1, and Z2. Figure A2 shows the ray tracing for Cases S1, Z1, and Z2. Figures A3, A4, and A5 show the backscatter power and the Fast Fourier Transform thereof for beam 15 of Case S1, beam 15 for Case Z1, and beam 12 for Case Z2, respectively. Figure A6 shows the Cross correlation between Near Range Echoes and Medium-Scale Traveling Ionospheric Disturbances for the cases presented in this article. Figures A7 and A8 are like Figure 6 in this article, but for Case Z1 and Z2, respectively.

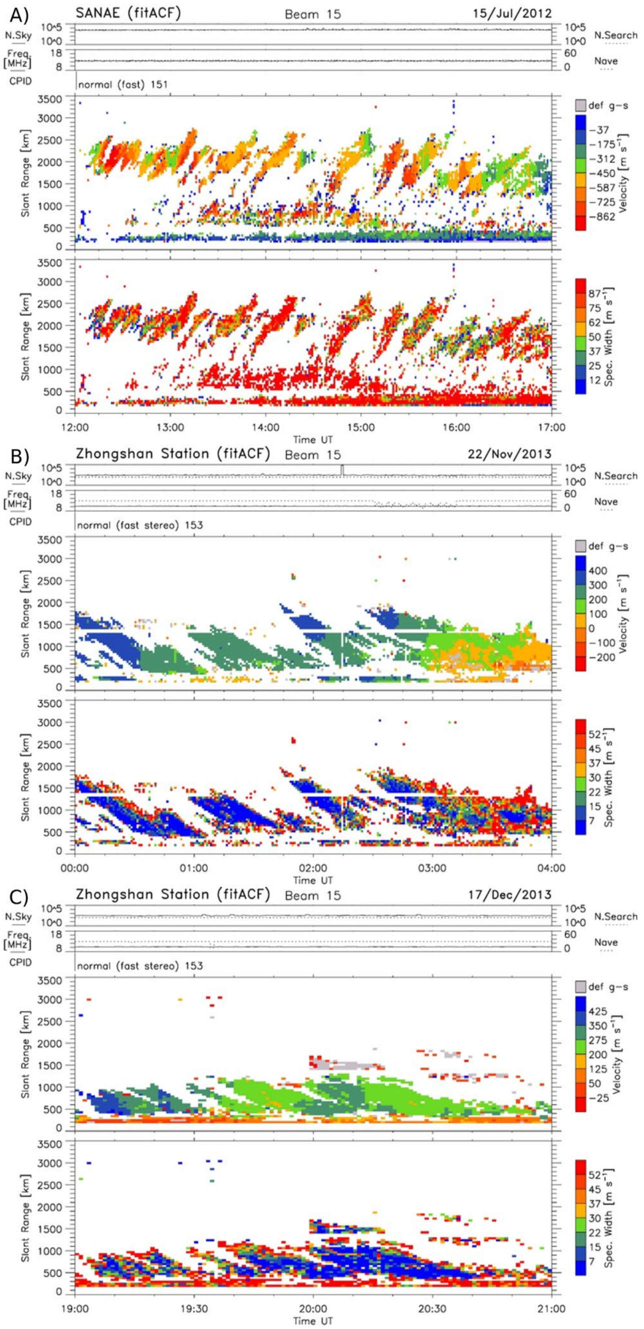

Figure A1. Range-Time-Intensity plot of Doppler velocity and spectra width of (a) beam 15 of the SANAE HF radar from 11:00 to 17:00 UT on 15 July 2012, (b) beam 15 of the Zhongshan HF radar from 00:00 to 04:00 UT on 22 November 2013, and (c) beam 15 of the Zhongshan HF radar from 19:00 to 21:00 UT on 17 December 2013. This figure complements Figure 3.

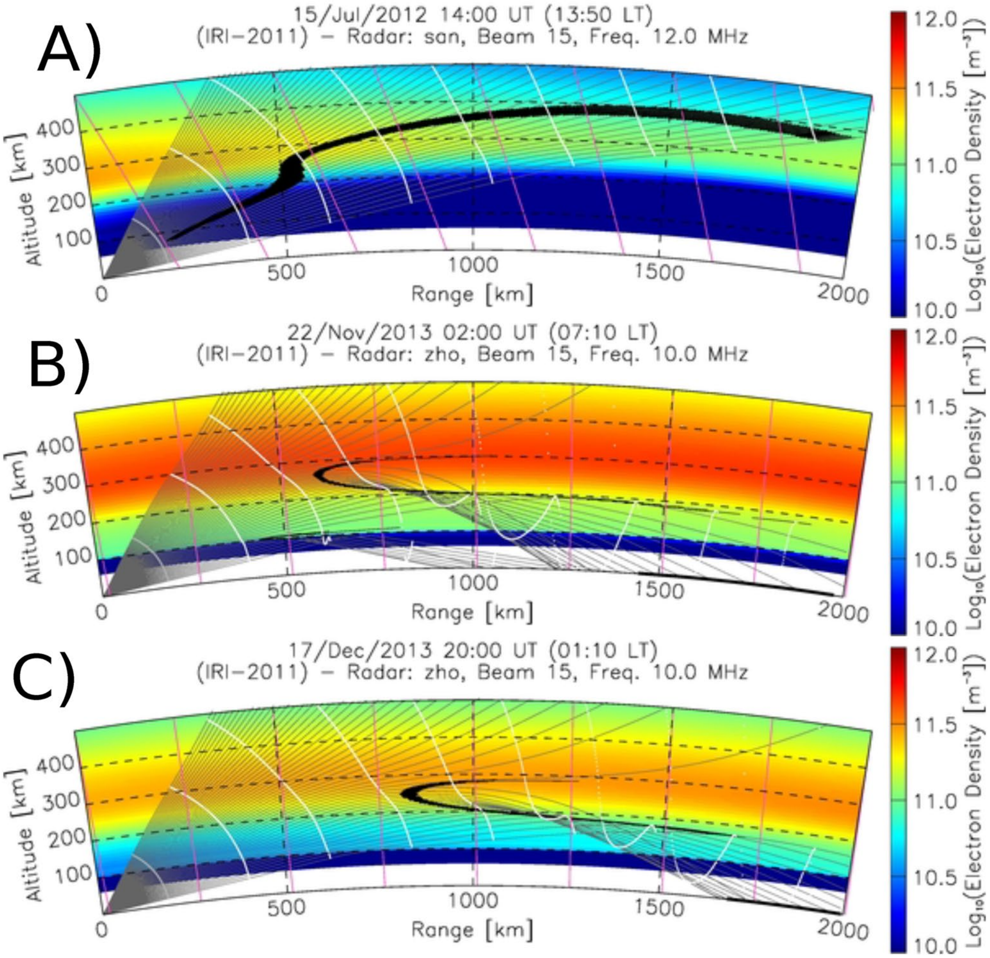

Figure A2. Ray tracing using the International Reference Ionosphere model at 12.0 MHz for SANAE and 10.0 MHz for Zhongshan. The locus of black points indicates where ionospheric and ground backscatter may be possible. Panel (a) is for 14:00 UT on 15 July 2012 (case S1), panel (b) is for 02:00 UT on 22 November 2013 (case Z1), and panel (c) is for 20:00 UT on 17 December 2013 (case Z2).

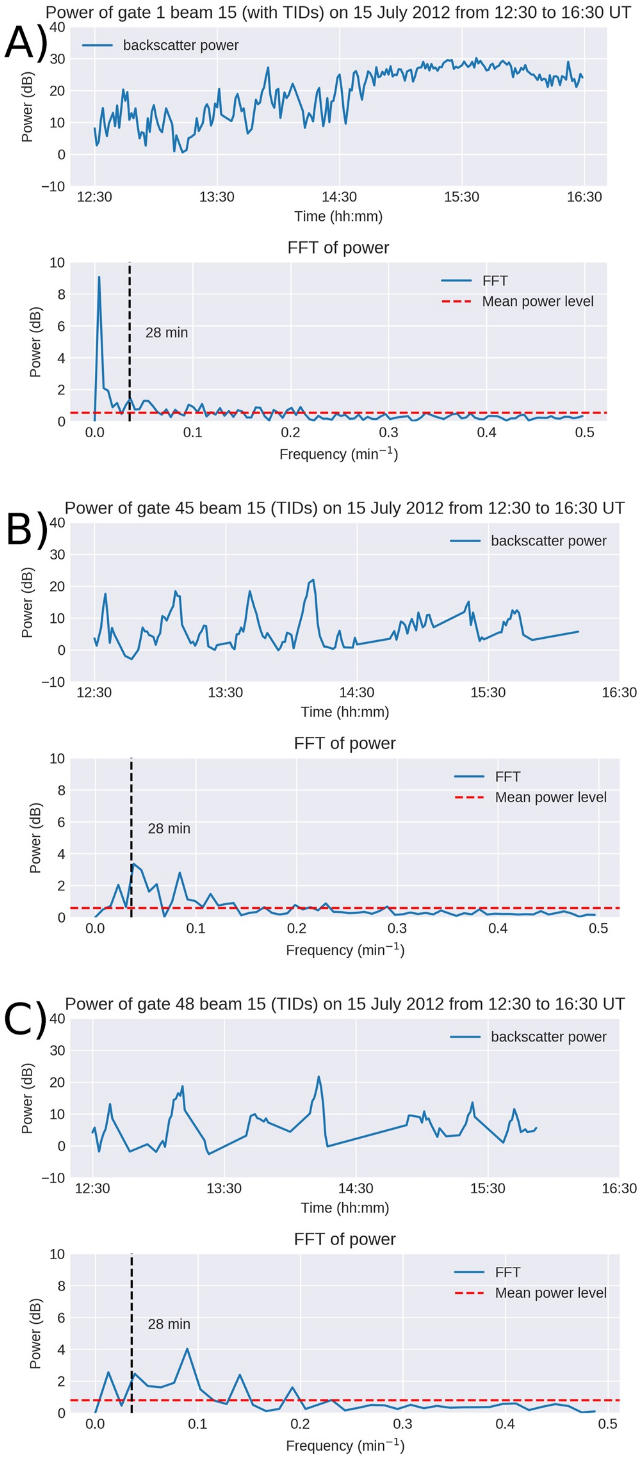

Figure A3. Backscatter power and the Fast Fourier Transform thereof for SANAE beam 15 on 15 July 2012 between 12:30 and 16:30 UT (case S1). Panel (a) is for gate 1 (Near Range Echoes). Panels (b and c) are for gates 45 and 48 (Medium-Scale Traveling Ionospheric Disturbances (MSTIDs)), respectively. The period of the MSTID is indicated (vertical dashed line).

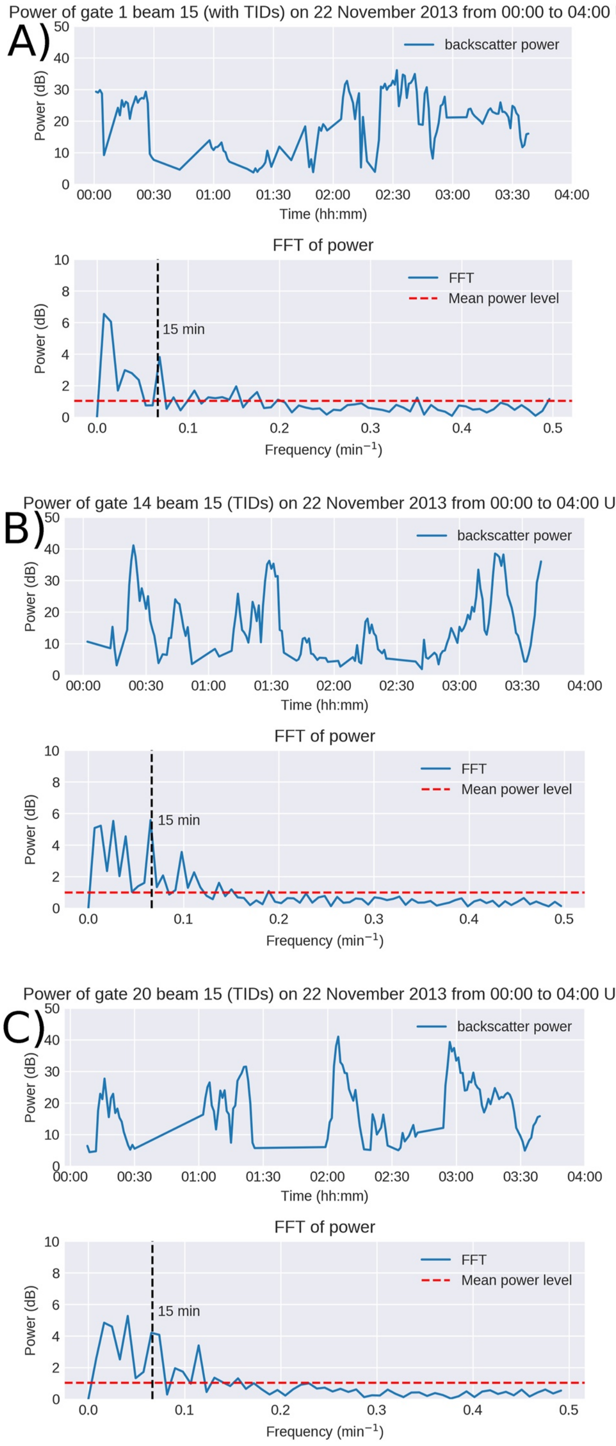

Figure A4. Backscatter power and the Fast Fourier Transform thereof for Zhongshan beam 15 on 22 November 2013 between 00:00 and 03:48 UT (case Z1). Panel (a) is for gate 1 (Near Range Echoes). Panels (b and c) are for gates 14 and 20 (Medium-Scale Traveling Ionospheric Disturbances (MSTIDs)). The period of the MSTID is indicated (vertical dashed line).

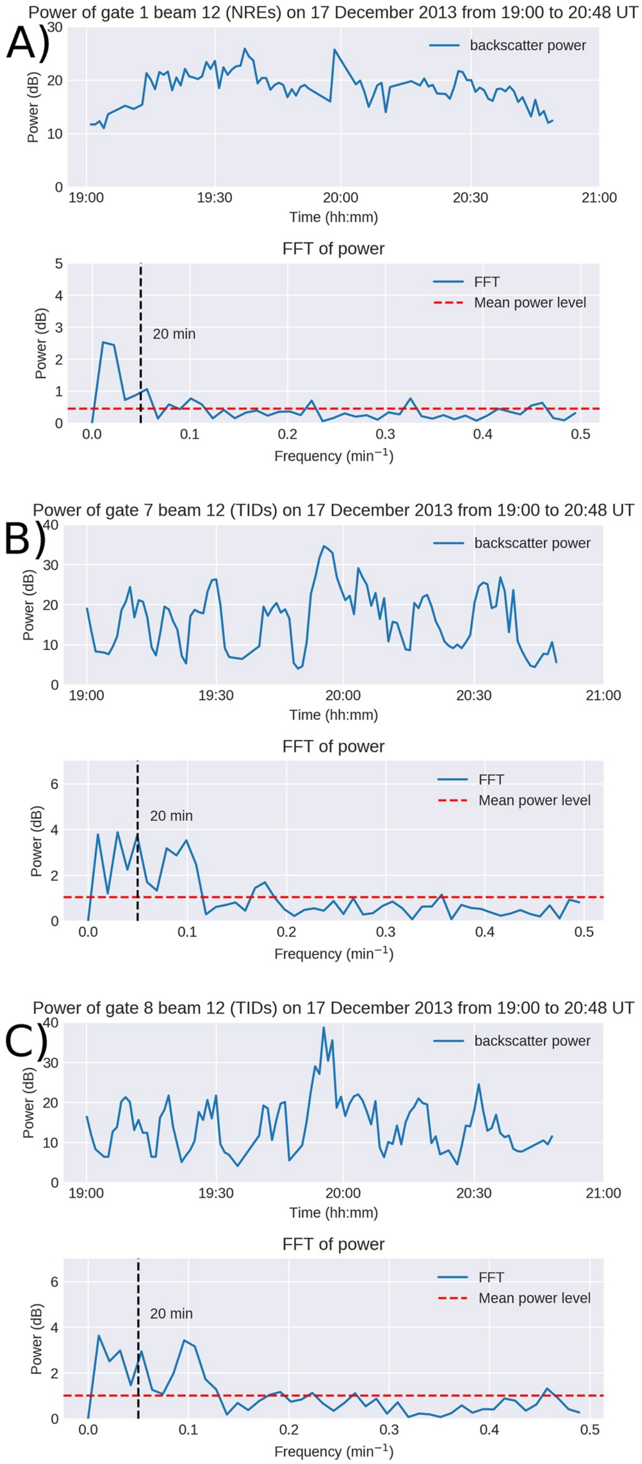

Figure A5. Backscatter power and the Fast Fourier Transform thereof for Zhongshan beam 12 on 17 December 2013 between 19:00 and 20:48 UT (case Z2). Panel (a) is for gate 1 (Near Range Echoes). Panels (b and c) are for gates 7 and 8 (Medium-Scale Traveling Ionospheric Disturbances (MSTIDs)). The period of the MSTID is indicated (vertical dashed line).

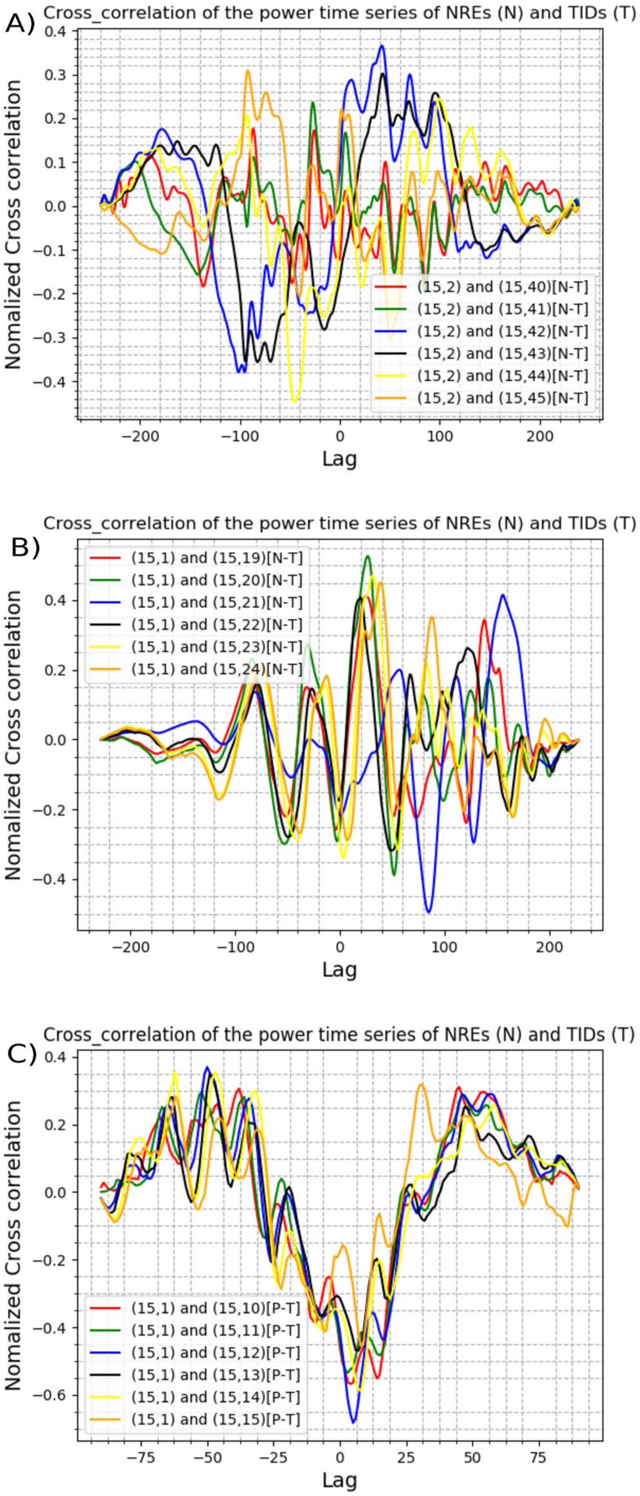

Figure A6. Cross correlation between Near Range Echoes and Medium-Scale Traveling Ionospheric Disturbances. Panel (a) is for SANAE beam 15 and gate 2 versus gates 40–45 on 15 July 2012 between 12:30 and 16:30 UT (case S1). Panel (b) is for Zhongshan beam 15 and gate 1 versus gates 19–24 on 22 November 2013 between 00:00 and 03:48 UT (case Z1). Panel (c) is for Zhongshan beam 15 and gate 1 versus gates 10–15 on 17 December 2013 between 19:00 and 20:48 UT (case Z2).

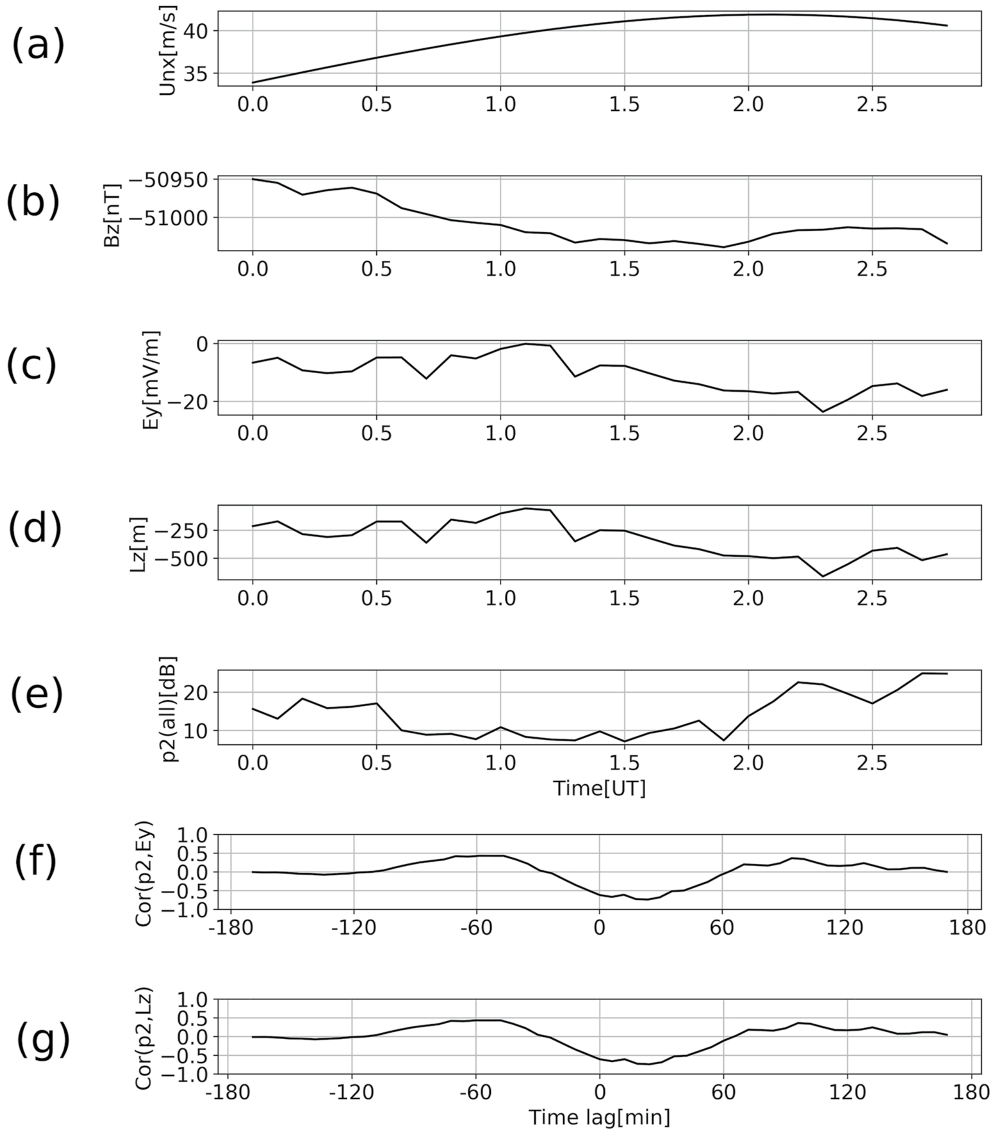

Figure A7. For 22 November 2013 from 00:00 to 02:48 UT at 100 km altitude (case Z1), (a) modeled eastward neutral wind, (b) Z-component of the Earth's magnetic field at ground level, (c) observed northward electric field (E_y), (d) calculated plasma density scale height (L_z), (e) the average backscatter power of all beams for range gate 2 ($p2$), (f) the cross correlation between E_y (panel c) and p2 (panel e), and (g) cross correlation between L_z (panel d) and $p2$ (panel e).

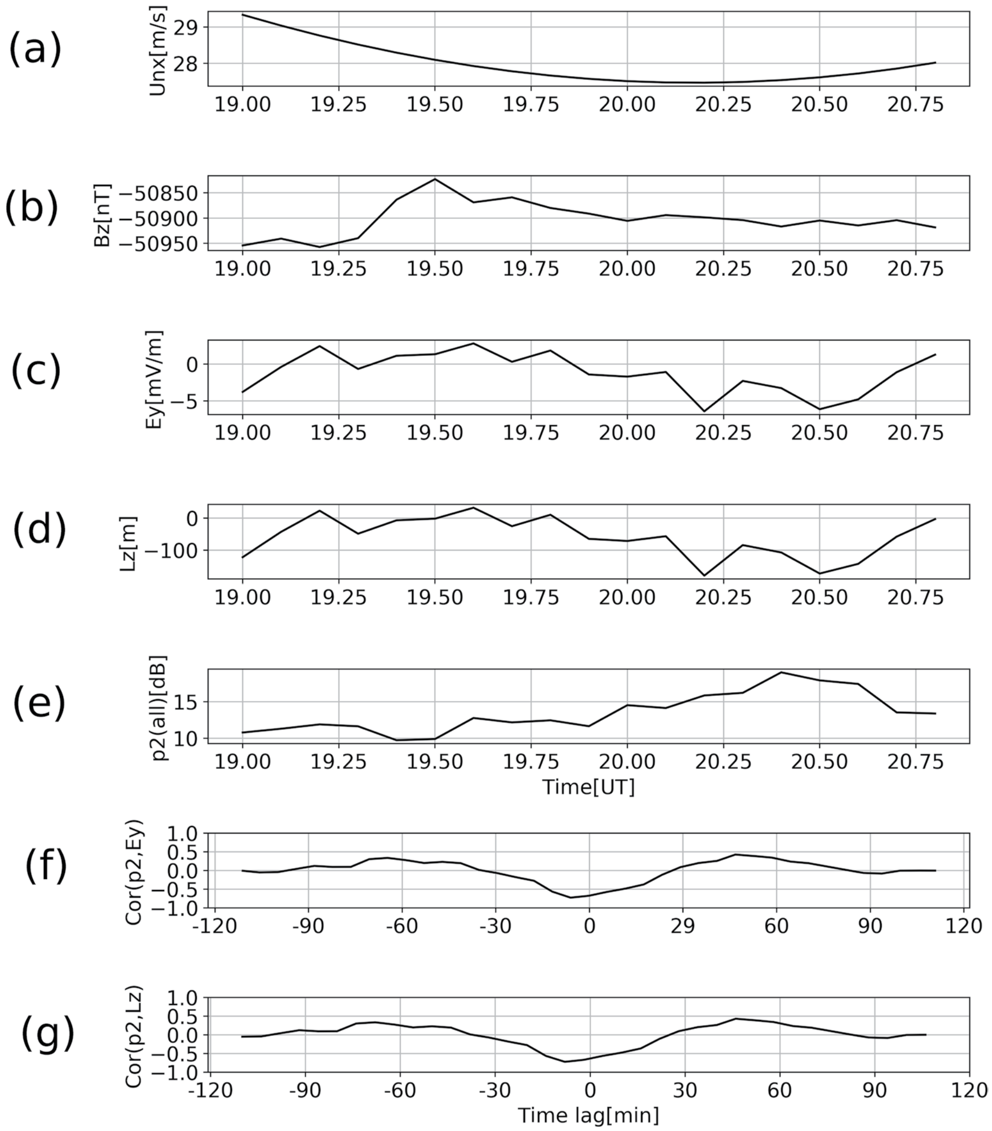

Figure A8. For 17 December 2013 from 19:00 to 20:48 UT at 100 km altitude (case Z2), (a) modeled eastward neutral wind, (b) Z-component of the Earth's magnetic field at ground level, (c) observed northward electric field (E_y), (d) calculated plasma density scale height (L_z), (e) the average backscatter power of all beams for range gate 2 (*p*2), (f) the cross correlation between E_y (panel c) and *p*2 (panel e), and (g) cross correlation between L_z (panel d) and *p*2 (panel e).

Acknowledgments

The authors acknowledge the South African National Space Agency (SANSA) and the South African National Antarctic Programme (SANAP) for supporting this research (NRF SANAP Grant 110742). The authors acknowledge the use of SuperDARN data. SuperDARN is a collection of radars funded by national scientific funding agencies of Australia, Canada, China, France, Italy, Japan, Norway, South Africa, United Kingdom, and the United States of America. The SuperDARN homepage link is http://vt.superdarn.org/tiki-index.php. Zhongshan magnetometer and ionosonde data were provided by the Beijing National Observatory of Space Environment, Institute of Geology and Geophysics Chinese Academy of Sciences through the Geophysics Center, National Earth System Science Data Center (http://wdc.geophys.ac.cn/). The authors would also like to thank MSIS-90, IRI-2016, and HWM-14 model developers. The authors thank the Zhongshan SuperDARN radar PI, Dr. Hongqiao Hu, for consenting to our use of the data, which is funded by the Polar Research Institute of China. The authors thank the NASA Goddard Space Flight Center, Space Physics Data Facility for providing ACE satellite and Magnetic Indices data through the OMNI website (https://omniweb.gsfc.nasa.gov/form/omni_min.html).

Data Availability Statement

The SANAE and Zhongshan SuperDARN fit data used in this study are available from the BAS SuperDARN data mirror https://www.bas.ac.uk/project/superdarn/#data or from the SuperDARN Virginia Tech web page http://vt.superdarn.org/tiki-index.php?page=Examine%20Fit%20Contents.

References

Atilaw, T. Y., Stephenson, J. A., & Katamzi-Joseph, Z. T. (2021). Multitaper analysis of an MSTID event above Antarctica on 17 March 2013. *Polar Science*, *28*, 100643. https://doi.org/10.1016/j.polar.2021.100643

Baker, K., Dudeney, J., Greenwald, R., Pinnock, M., Newell, P., Rodger, A., et al. (1995). HF radar signatures of the cusp and low-latitude boundary layer. *Journal of Geophysical Research*, *100*(A5), 7671–7695. https://doi.org/10.1029/94JA01481

Bilitza, D., Altadill, D., Truhlik, V., Shubin, V., Galkin, I., Reinisch, B., & Huang, X. (2017). International Reference Ionosphere 2016: From ionospheric climate to real-time weather predictions. *Space Weather*, *15*(2), 418–429. https://doi.org/10.1002/2016SW001593

Bowman, G. (1960). Some aspects of sporadic-E at mid-latitudes. *Planetary and Space Science*, *2*(4), 195–202. https://doi.org/10.1016/0032-0633(60)90016-7

Bowman, G. (1968). Movements of ionosphereic irregularities and gravity waves. *Journal of Atmospheric and Terrestrial Physics*, *30*(5), 721–734. https://doi.org/10.1016/S0021-9169(68)80028-5

Chisham, G., & Freeman, M. P. (2013). A reassessment of SuperDARN meteor echoes from the upper mesosphere and lower thermosphere. *Journal of Atmospheric and Solar-Terrestrial Physics*, *102*, 207–221. https://doi.org/10.1016/j.jastp.2013.05.018

Chisham, G., Lester, M., Milan, S., Freeman, M., Bristow, W., Grocott, A., et al. (2007). A decade of the Super Dual Auroral Radar Network (SuperDARN): Scientific achievements, new techniques and future directions. *Surveys in Geophysics*, *28*(1), 33–109. https://doi.org/10.1007/s10712-007-9017-8

Dalin, P., Kirkwood, S., Moström, A., Stebel, K., Hoffmann, P., & Singer, W. (2004). A case study of gravity waves in noctilucent clouds. In *Annales Geophysicae* (Vol. 22, No. 6, pp. 1875–1884). https://doi.org/10.5194/angeo-22-1875-2004

Ding, F., Wan, W., Liu, L., Afraimovich, E., Voeykov, S., & Perevalova, N. (2008). A statistical study of large-scale traveling ionospheric disturbances observed by GPS TEC during major magnetic storms over the years 2003–2005. *Journal of Geophysical Research*, *113*(A3). https://doi.org/10.1029/2008JA013037

Drexler, J., & St-Maurice, J.-P. (2005). A possible origin for large aspect angle (HAIR) echoes seen by SuperDARN radars in the E region. In *Annales Geophysicae* (Vol. 23, No. 3, pp. 767–772). https://doi.org/10.5194/angeo-23-767-2005

Drob, D. P., Emmert, J. T., Meriwether, J. W., Makela, J. J., Doornbos, E., Conde, M., et al. (2015). An update to the Horizontal Wind Model (HWM): The quiet time thermosphere. *Earth and Space Science*, *2*(7), 301–319. https://doi.org/10.1002/2014EA000089

Farley, D., Jr. (1960). A theory of electrostatic fields in the ionosphere at nonpolar geomagnetic latitudes. *Journal of Geophysical Research*, *65*(3), 869–877. https://doi.org/10.1029/JZ065i003p00869

Fejer, B. G., Providakes, J., & Farley, D. T. (1984). Theory of plasma waves in the auroral E region. *Journal of Geophysical Research*, *89*(A9), 7487–7494. https://doi.org/10.1029/JA089iA09p07487

Fiori, R., Boteler, D., Knudsen, D., Burchill, J., Koustov, A., Cousins, E., & Blais, C. (2013). Potential impact of Swarm electric field data on global 2D convection mapping in combination with SuperDARN radar data. *Journal of Atmospheric and Solar-Terrestrial Physics*, *93*, 87–99. https://doi.org/10.1016/j.jastp.2012.11.013

Francis, S. H. (1974). A theory of medium-scale traveling ionospheric disturbances. *Journal of Geophysical Research*, *79*(34), 5245–5260. https://doi.org/10.1029/JA079i034p05245

Francis, S. H. (1975). Global propagation of atmospheric gravity waves: A review. *Journal of Atmospheric and Terrestrial Physics*, *37*(6–7), 1011–1054. https://doi.org/10.1016/0021-9169(75)90012-4

Fritts, D. C. (1984). Gravity wave saturation in the middle atmosphere: A review of theory and observations. *Reviews of Geophysics*, *22*(3), 275–308. https://doi.org/10.1029/RG022i003p00275

Gillies, D. (2012). *Global-scale observations of changes in ionospheric echo occurrence and convection during periods of increased solar wind activity and increased geomagnetic activity* (Unpublished doctoral dissertation). University of Saskatchewan.

Gondarenko, N., & Guzdar, P. (2001). Three-dimensional structuring characteristics of high-latitude plasma patches. *Journal of Geophysical Research*, *106*(A11), 24611–24620. https://doi.org/10.1029/2000JA000440

Goodwin, G. (1966). The dimensions of some horizontally-moving Es-region irregularities. *Planetary and Space Science*, *14*(8), 759–771. https://doi.org/10.1016/0032-0633(66)90105-X

Greenwald, R., Baker, K., Dudeney, J., Pinnock, M., Jones, T., Thomas, E., et al. (1995). Darn/SuperDARN. *Space Science Reviews*, *71*(1–4), 761–796. https://doi.org/10.1007/BF00751350

Grocott, A., Hosokawa, K., Ishida, T., Lester, M., Milan, S., Freeman, M., et al. (2013). Characteristics of medium-scale traveling ionospheric disturbances observed near the Antarctic Peninsula by HF radar. *Journal of Geophysical Research: Space Physics*, *118*(9), 5830–5841. https://doi.org/10.1002/jgra.50515

Habarulema, J. B., Katamzi, Z. T., & Yizengaw, E. (2015). First observations of poleward large-scale traveling ionospheric disturbances over the African sector during geomagnetic storm conditions. *Journal of Geophysical Research: Space Physics*, *120*(8), 6914–6929. https://doi.org/10.1002/2015JA021066

Haldoupis, C., Kelley, M. C., Hussey, G. C., & Shalimov, S. (2003). Role of unstable sporadic-E layers in the generation of midlatitude spread F. *Journal of Geophysical Research*, *108*(A12), 1446. https://doi.org/10.1029/2003JA009956

Haldoupis, C., Schlegel, K., & Hussey, G. (2000). Auroral E-region electron density gradients measured with EISCAT. In *Annales Geophysicae* (Vol. 18, No. 9, pp. 1172–1181). https://doi.org/10.1007/s005850000223

Hall, G., MacDougall, J., Moorcroft, D., St.-Maurice, J.-P., Manson, A., & Meek, C. (1997). Super Dual Auroral Radar Network observations of meteor echoes. *Journal of Geophysical Research*, *102*(A7), 14603–14614. https://doi.org/10.1029/97JA00517

Hayashi, H., Nishitani, N., Ogawa, T., Otsuka, Y., Tsugawa, T., Hosokawa, K., & Saito, A. (2010). Large-scale traveling ionospheric disturbance observed by SuperDARN Hokkaido HF radar and GPS networks on 15 December 2006. *Journal of Geophysical Research*, *115*(A6). https://doi.org/10.1029/2009JA014297

He, L.-S., Dyson, P., Parkinson, M., & Wan, W. (2004). Studies of medium scale travelling ionospheric disturbances using TIGER SuperDARN radar sea echo observations. In *Annales Geophysicae* (Vol. 22, No. 12, pp. 4077–4088). https://doi.org/10.5194/angeo-22-4077-2004

Hedin, A. (1988). The atmospheric model in the region 90 to 2000 km. *Advances in Space Research*, *8*(5–6), 9–25. https://doi.org/10.1016/0273-1177(88)90038-5

Hernández-Pajares, M., Juan, J. M., & Sanz, J. (2006). Medium-scale traveling ionospheric disturbances affecting GPS measurements: Spatial and temporal analysis. *Journal of Geophysical Research*, *111*(A7), A07S11. https://doi.org/10.1029/2005JA011474

Hocke, K., & Schlegel, K. (1996). A review of atmospheric gravity waves and travelling ionospheric disturbances: 1982–1995. In *Annales Geophysicae* (Vol. 14, No. 9, pp. 917–940). https://doi.org/10.1007/s00585-996-0917-6

Hosokawa, K., Ogawa, T., Arnold, N., Lester, M., Sato, N., & Yukimatu, A. (2005). Extraction of polar mesosphere summer echoes from SuperDARN data. *Geophysical Research Letters*, *32*(12). https://doi.org/10.1029/2005GL022788

Hunsucker, R. D. (1982). Atmospheric gravity waves generated in the high-latitude ionosphere: A review. *Reviews of Geophysics*, *20*(2), 293–315. https://doi.org/10.1029/RG020i002p00293

Hussey, G., Meek, C., André, D., Manson, A., Sofko, G., & Hall, C. (2000). A comparison of Northern Hemisphere winds using SuperDARN meteor trail and MF radar wind measurements. *Journal of Geophysical Research*, *105*(D14), 18053–18066. https://doi.org/10.1029/2000JD900272

Jenkins, B., & Jarvis, M. J. (1999). Mesospheric winds derived from SuperDARN HF radar meteor echoes at Halley, Antarctica. *Earth Planets and Space*, *51*(7–8), 685–689. https://doi.org/10.1186/BF03353226

Kagan, L. M., & Kelley, M. C. (1998). A wind-driven gradient drift mechanism for mid-latitude E-region ionospheric irregularities. *Geophysical Research Letters*, *25*(22), 4141–4144. https://doi.org/10.1029/1998GL900123

Kavanagh, A., Honary, F., Rietveld, M., & Senior, A. (2006). First observations of the artificial modulation of polar mesospheric winter echoes. *Geophysical Research Letters*, *33*(19), L19801. https://doi.org/10.1029/2006GL027565

Kelley, M. C. (2009). *The Earth's ionosphere: Plasma physics and electrodynamics*. Academic Press.

Kelly, M. (2012). *The Earth's Ionosphere: Plasma Physics and Electrodynamics* (Vol. 43). Elsevier.

Keskinen, M., & Ossakow, S. (1983). Theories of high-latitude ionospheric irregularities: A review. *Radio Science*, *18*(06), 1077–1091. https://doi.org/10.1029/RS018i006p01077

Kirkwood, S., & Von Zahn, U. (1991). On the role of auroral electric fields in the formation of low altitude sporadic-E and sudden sodium layers. *Journal of Atmospheric and Terrestrial Physics*, *53*(5), 389–407. https://doi.org/10.1016/0021-9169(91)90034-5

Kotake, N., Otsuka, Y., Ogawa, T., Tsugawa, T., & Saito, A. (2007). Statistical study of medium-scale traveling ionospheric disturbances observed with the GPS networks in Southern California. *Earth Planets and Space*, *59*(2), 95–102. https://doi.org/10.1186/BF03352681

Kotzé, P. B. (2018). Hermanus magnetic observatory: A historical perspective of geomagnetism in southern Africa. *History of Geo-and Space Sciences*, *9*(2), 125–131. https://doi.org/10.5194/hgss-9-125-2018

Li, H.-L., Wu, J., Liu, R.-Y., & Huang, J.-Y. (2007). Study on mesosphere summer echoes observed by digital ionosonde at Zhongshan Station, Antarctica. *Earth Planets and Space*, *59*(10), 1135–1139. https://doi.org/10.1186/BF03352056

Liu, E., Hu, H., Hosokawa, K., Liu, R., Wu, Z., & Xing, Z. (2013). First observations of polar mesosphere summer echoes by SuperDARN Zhongshan radar. *Journal of Atmospheric and Solar-Terrestrial Physics*, *104*, 39–44. https://doi.org/10.1016/j.jastp.2013.07.011

Liu, Y., Hu, H., Yang, H., Zhang, B., Sun, B., Wei, F., et al. (2016). Chinese Antarctic magnetometer chain at the cusp latitude. *Advances in Polar Science*, *27*(2), 102–106. https://doi.org/10.13679/j.advps.2016.2.00102

Liu, Y., Zhou, C., Tang, Q., Kong, J., Gu, X., Ni, B., et al. (2019). Evidence of mid-and low-latitude nighttime ionospheric *E–F* coupling: Coordinated observations of sporadic *E* layers, *F*-region field-aligned irregularities, and medium-scale traveling ionospheric disturbances. *IEEE Transactions on Geoscience and Remote Sensing*, *57*(10), 7547–7557. https://doi.org/10.1109/TGRS.2019.2914059

Makarevich, R. A. (2014). Symmetry considerations in the two-fluid theory of the gradient drift instability in the lower ionosphere. *Journal of Geophysical Research: Space Physics*, *119*(9), 7902–7913. https://doi.org/10.1002/2014JA020292

Miyoshi, Y., Jin, H., Fujiwara, H., & Shinagawa, H. (2018). Numerical study of traveling ionospheric disturbances generated by an upward propagating gravity wave. *Journal of Geophysical Research: Space Physics*, *123*(3), 2141–2155. https://doi.org/10.1002/2017JA025110

Nishitani, N., Ogawa, T., Otsuka, Y., Hosokawa, K., & Hori, T. (2011). Propagation of large amplitude ionospheric disturbances with velocity dispersion observed by the SuperDARN Hokkaido radar after the 2011 off the Pacific coast of Tohoku Earthquake. *Earth Planets and Space*, *63*(7), 891–896. https://doi.org/10.5047/eps.2011.07.003

Nishitani, N., Ruohoniemi, J. M., Lester, M., Baker, J. B. H., Koustov, A. V., Shepherd, S. G., et al. (2019). Review of the accomplishments of mid-latitude Super Dual Auroral Radar Network (SuperDARN) HF radars. *Progress in Earth and Planetary Science*, *6*(1), 1–57. https://doi.org/10.1186/s40645-019-0270-5

Ogawa, T., Igarashi, K., Aikyo, K., & Maeno, H. (1987). NNSS satellite observations of medium-scale traveling ionospheric disturbances at southern high-latitudes. *Journal of Geomagnetism and Geoelectricity*, *39*(12), 709–721. https://doi.org/10.5636/jgg.39.709

Ogawa, T., Nishitani, N., Otsuka, Y., Shiokawa, K., Tsugawa, T., & Hosokawa, K. (2009). Medium-scale traveling ionospheric disturbances observed with the SuperDARN Hokkaido radar, all-sky imager, and GPS network and their relation to concurrent sporadic E irregularities. *Journal of Geophysical Research*, *114*(A3). https://doi.org/10.1029/2008JA013893

Ogunjobi, O., Sivakumar, V., Stephenson, E., Ann, J., & Mtumela, Z. (2017). PMSE long term observations using SuperDARN SANAE HF radar measurements. *Terrestrial, Atmospheric and Oceanic Sciences*, *28*(3), 371–383. https://doi.org/10.3319/TAO.2016.09.19.01

Ogunjobi, O., Sivakumar, V., Stephenson, J. A. E., & Sivla, W. T. (2015). Evidence of polar mesosphere summer echoes observed by SuperDARN SANAE HF radar in Antarctica. *Terrestrial, Atmospheric and Oceanic Sciences*, *26*(4), 431. https://doi.org/10.3319/TAO.2015.03.06.01(AA)

Oinats, A. V., Kurkin, V. I., & Nishitani, N. (2015). Statistical study of medium-scale traveling ionospheric disturbances using SuperDARN Hokkaido ground backscatter data for 2011. *Earth Planets and Space*, *67*(1), 22. https://doi.org/10.1186/s40623-015-0192-4

Otsuka, Y., Onoma, F., Shiokawa, K., Ogawa, T., Yamamoto, M., & Fukao, S. (2007). Simultaneous observations of nighttime medium-scale traveling ionospheric disturbances and E region field-aligned irregularities at midlatitude. *Journal of Geophysical Research*, *112*(A6). https://doi.org/10.1029/2005JA011548

Otsuka, Y., Shiokawa, K., Ogawa, T., & Wilkinson, P. (2004). Geomagnetic conjugate observations of medium-scale traveling ionospheric disturbances at midlatitude using all-sky airglow imagers. *Geophysical Research Letters*, *31*(15), L15803. https://doi.org/10.1029/2004GL020262

Otsuka, Y., Shiokawa, K., Ogawa, T., Yokoyama, T., & Yamamoto, M. (2009). Spatial relationship of nighttime medium-scale traveling ionospheric disturbances and F region field-aligned irregularities observed with two spaced all-sky airglow imagers and the middle and upper atmosphere radar. *Journal of Geophysical Research*, *114*(A5). https://doi.org/10.1029/2008JA013902

Palmroth, M., Janhunen, P., Pulkkinen, T., Aksnes, A., Lu, G., Østgaard, N., et al. (2005). Assessment of ionospheric Joule heating by GUMICS-4 MHD simulation, AMIE, and satellite-based statistics: Towards a synthesis. In *Annales Geophysicae* (Vol. 23, No. 6, pp. 2051–2068). https://doi.org/10.5194/angeo-23-2051-2005

Ponomarenko, P. V., Iserhienrhien, B., & Maurice, J.-P. S. (2016). Morphology and possible origins of near-range oblique HF backscatter at high and midlatitudes. *Radio Science*, *51*(6), 718–730. https://doi.org/10.1002/2016RS006088

Ponomarenko, P. V., St-Maurice, J., Waters, C., Gillies, R., & Koustov, A. (2009). Refractive index effects on the scatter volume location and Doppler velocity estimates of ionospheric HF backscatter echoes. In *Annales Geophysicae* (Vol. 27, No. 11, pp. 4207–4219). https://doi.org/10.5194/angeo-27-4207-2009

Ponomarenko, P. V., & Waters, C. (2006). Spectral width of SuperDARN echoes: Measurement, use and physical interpretation. In *Annales Geophysicae* (Vol. 24, No. 1, pp. 115–128). https://doi.org/10.5194/angeo-24-115-2006

Ruohoniemi, J., Greenwald, R., Baker, K., Villain, J.-P., Hanuise, C., & Kelly, J. (1989). Mapping high-latitude plasma convection with coherent HF radars. *Journal of Geophysical Research*, *94*(A10), 13463–13477. https://doi.org/10.1029/JA094iA10p13463

Samson, J., Greenwald, R., Ruohoniemi, J., Frey, A., & Baker, K. (1990). Goose Bay radar observations of Earth-reflected, atmospheric gravity waves in the high-latitude ionosphere. *Journal of Geophysical Research*, *95*(A6), 7693–7709. https://doi.org/10.1029/JA095iA06p07693

Senior, A., Kosch, M., Yeoman, T. K., Rietveld, M., & McCrea, I. (2006). Effects of high-latitude atmospheric gravity wave disturbances on artificial HF radar backscatter. In *Annales Geophysicae* (Vol. 24, No. 9, pp. 2347–2361). https://doi.org/10.5194/angeo-24-2347-2006

Shepherd, S., & Ruohoniemi, J. (2000). Electrostatic potential patterns in the high-latitude ionosphere constrained by SuperDARN measurements. *Journal of Geophysical Research*, *105*(A10), 23005–23014. https://doi.org/10.1029/2000JA000171

Sojka, J. J., Subramanium, M., Zhu, L., & Schunk, R. (1998). Gradient drift instability growth rates from global-scale modeling of the polar ionosphere. *Radio Science*, *33*(6), 1915–1928. https://doi.org/10.1029/98RS02490

St.-Maurice, J.-P. (1985). A nonlocal theory of the high-latitude Farley-Buneman Instability. *Journal of Geophysical Research*, *90*(A6), 5211–5225. https://doi.org/10.1029/JA090iA06p05211

St.-Maurice, J.-P., & Nishitani, N. (2020). On the origin of far-aspect angle irregularity regions seen by HF radars at 100-km altitude. *Journal of Geophysical Research: Space Physics*, *125*(6), e2019JA027473. https://doi.org/10.1029/2019JA027473

Sun, L., Xu, J., Wang, W., Yue, X., Yuan, W., Ning, B., et al. (2015). Mesoscale field-aligned irregularity structures (FAIs) of airglow associated with medium-scale traveling ionospheric disturbances (MSTIDs). *Journal of Geophysical Research: Space Physics*, *120*(11), 9839–9858. https://doi.org/10.1002/2014JA020944

Suzuki, S., Hosokawa, K., Otsuka, Y., Shiokawa, K., Ogawa, T., Nishitani, N., et al. (2009). Coordinated observations of nighttime medium-scale traveling ionospheric disturbances in 630-nm airglow and HF radar echoes at midlatitudes. *Journal of Geophysical Research*, *114*(A7). https://doi.org/10.1029/2008JA013963

Tsugawa, T., Saito, A., & Otsuka, Y. (2004). A statistical study of large-scale traveling ionospheric disturbances using the GPS network in Japan. *Journal of Geophysical Research*, *109*(A6), A06302. https://doi.org/10.1029/2003JA010302

Tsunoda, R. T., & Cosgrove, R. B. (2001). Coupled electrodynamics in the nighttime midlatitude ionosphere. *Geophysical Research Letters*, *28*(22), 4171–4174. https://doi.org/10.1029/2001GL013245

Tsunoda, R. T., Fukao, S., & Yamamoto, M. (1994). On the origin of quasi-periodic radar backscatter from midlatitude sporadic E. *Radio Science*, *29*(01), 349–365. https://doi.org/10.1029/93RS01511

Waldock, J., & Jones, T. (1986). HF Doppler observations of medium-scale travelling ionospheric disturbances at mid-latitudes. *Journal of Atmospheric and Terrestrial Physics*, *48*(3), 245–260. https://doi.org/10.1016/0021-9169(86)90099-1

Woodman, R., Yamamoto, M., & Fukao, S. (1991). Gravity wave modulation of gradient drift instabilities in mid-latitude sporadic E irregularities. *Geophysical Research Letters*, *18*(7), 1197–1200. https://doi.org/10.1029/91GL01159

Zhou, C., Tang, Q., Huang, F., Liu, Y., Gu, X., Lei, J., et al. (2018). The simultaneous observations of nighttime ionospheric E region irregularities and F region medium-scale traveling ionospheric disturbances in midlatitude China. *Journal of Geophysical Research: Space Physics*, *123*(6), 5195–5209. https://doi.org/10.1029/2018JA025352